NASA Contractor Report 181871

AN EVALUATION OF THREE EXPERIMENTAL PROCESSES FOR TWO-DIMENSIONAL TRANSONIC TESTS

Gennaro ZUPPARDI

NASA

SUMMARY

Aerodynamic measurements in conventional wind tunnels suffer from the interference effects of the sting supporting the model and the test section walls. These effects are particularly severe at transonic speeds where they can significantly affect the aerodynamic measurements.

Sting interference can be completely overcome by using Magnetic Suspension techniques. Wall interference can be reduced by; testing airfoils in conventional, ventilated tunnels at relatively small model to tunnel size ratios, treatment of the tunnel wall boundary layers, or by using Adaptive Wall Test Sections (AWTS).

This paper assesses the operating capabilities and results from two of the foremost two-dimensional, transonic, AWTS tunnels in existence. These are the NASA Langley 0.3-m Transonic Cryogenic Tunnel and the ONERA-CERT T-2 tunnel in Toulouse, France. In addition, this paper evaluates the results derived from the well known conventional Canadian facility, the NAE 5' x 5' wind tunnel. The CAST 10/DOA2 Airfoil results are used in all of the evaluations.

CONTENTS

LIST OF ILLUSTRATIONS

LIST OF TABLES

A	non-dimensional cross sectional area of an airfoil
a, b	intercept and slope of a least square linear fit
c	model chord
C_d	drag coefficient
C_l	lift coefficient
$C_{l\alpha}$	lift curve slope
C_n	normal force coefficient
C_p	pressure coefficient
CF	coupling factor (CF=0.35)
F	cubic spline function of the pressure coefficients
k	ratio of the specific heats
L, H, W	length, height and width of the test section
M	Mach number
N	iterations number
P	stagnation pressure
p, q	independent flow variables
Q	weighing function
R_c	Reynolds number based on model chord
R_m	Reynolds number per meter
r	correlation coefficient of a least square linear fit
SF	scaling factor (SF=0.8)
T	stagnation temperature
T_a	ambient temperature
U	velocity along the tunnel axis
u, v	streamwise and normal components of the perturbation velocity
V	local velocity parallel to the wall
V_s	BLC suction velocity
X, Z	wall/jack coordinates
X_B, X_E	integration limits of the wall adaptation strategies
X_L, X_U	pressure measurement limits of the ONERA T-2 tunnel
x, z	airfoil coordinates
x', y'	tunnel reference system of the Mokry's technique
Y	spanwise coordinate of the test section
α	angle of attack
β	Prandtl-Glauert coefficient
γ	vorticity strength
$\Delta\alpha$	correction to angle of attack
ΔC_l	deviation from linear lift curve
ΔM	correction to Mach number
$\Delta u, \Delta v$	corrections to the components of the perturbation velocity
ΔZ	wall/jack aerodynamic movement
ΔZ_w	wall/jack actual movement
ΔZ_Σ	distance between Σ and the wall
δ^*	boundary layer displacement thickness
ϵ	convergence criterion
ζ	coordinate along Σ
μ	doublet strength
ξ	non-jack coordinate along the representation plane of the wall
ξ', η'	reduced coordinates of the Mokry's method
Σ	control plane near the wall
φ	potential of the perturbation velocity
ψ	flow angle
ω	weighing factor

Subscripts

C, F	ceiling, floor
c	compressible
f	imaginary
i	incompressible
n	number of streamlining jacks
r	real
s	shock
sw	sidewall
w	wall interference
∞	free stream

Superscripts

I	Ith iteration step
p	weighed
w'	wall projection

Special Symbols

AWTS	adaptive wall test section
BL	boundary layer
BLC	sidewall boundary layer control system
DGT/IGT	direct/inverse green transform
GN_2/LN_2	gaseous/liquid nitrogen

1. INTRODUCTION

The aerodynamic measurements in conventional wind tunnels suffer from the interference effects of: the sting supporting the model and the test section walls. These effects are particularly severe at transonic speeds where they can significantly affect the aerodynamic measurements.

Sting interference can be overcome by using Magnetic Suspension techniques (Ref. 1). This technique allows the researcher to test models without any physical support or contact with the tunnel.

Tunnel wall interference has been typically alleviated by decreasing the solid blockage by physical methods or by applying analytical corrections. The decrease of the solid blockage involves:

1) Enlarging the test section. This, obviously, increases the initial investment, and the operating and maintenance costs of the facility.

2) Reducing the size of the model. This often decreases the test Reynolds number to unacceptable values.

The effective use of the corrective methods is restricted to *correctable* flow fields. A flow field is correctable when we can consider that in the region of the model both the streamwise (u_w) and the normal (v_w) component of the wall interference velocity are constant. For correctable flows we can achieve a strict equivalence of the free air and the constricted flow fields. Simple formulas are available to compute, in subsonic flows, the correction terms Δu_w and Δv_w to u_w and v_w, respectively (Ref. 2). The computation of Δu_w, Δv_w in transonic flows suffers from several drawbacks:

1) It requires powerful computers and time consuming procedures. In addiction, the corrected data are usually not available at the end of the test because the complexity requires correcting the data after the testing is finished (post run processing).

2) The inability to establish accurately the boundary conditions on ventilated (slotted and/or perforated) test sections increases the computational difficulty.

3) The corrections are unreliable when the test is performed under operating conditions not matching the theoretical hypothesis of the correcting method.

The Adaptive Wall Test Section (AWTS) can overcome the above mentioned disadvantages. This type of facility minimizes the solid blockage without physically increasing the test section size or decreasing the model size. The AWTS eliminates or reduces to correctable values the induced wall interference velocity.

The concept of the AWTS is not recent (Ref. 3). It was developed around 1937. Researchers built the first AWTS (12.7 cm x 5.08 cm) with a flexible ceiling and floor at the National Physical Laboratory (England) in 1937-38. Even though the tests were encouraging, adaptive wall researches did not continue beyond the 1950s. This was due probably to the lack of computing power and the advent of ventilated test sections for transonic tunnels. The lack of computing power involved manual operation of the adaptive procedure and therefore lengthy and laborious working.

The interest in the AWTS was renewed in the early 1970s. Both computers and technology were ready to allow full-automatic AWTS operation. New and more sophisticated adaptation strategies were developed.

Several such facilities were built both in Europe (England, France, Germany) and in the United States. In 1982 Ashill (Ref. 4) quantified the benefits of the AWTS over the conventional rigid wall wind tunnel in reducing the wall interference. He computed the correction terms Δu_w and Δv_w from two sets of data for a NACA 0012 airfoil. This airfoil was tested in the ONERA T-2 tunnel at several test conditions. One set of data was obtained with straight walls and the other one with adapted walls. Typically, for the test case $M_\infty = 0.73$ and $\alpha = 0$, the computations showed that the variation along the model chord of both the streamwise and the normal wall interference velocities were substantially smaller for the adapted walls. The correction to Mach number (that is, to u_w) was 0.023 and 0.002 for the measurements with straight and adapted walls, respectively. The correction to angle of attack (that is, to v_w) was -0.007 and 0.005 for the measurements with straight and adapted walls, respectively. These advantages over conventional tunnels allow the AWTS to become a unique test facility for making accurate 2-D transonic tests.

The purpose of the present study is to assess the operating capabilities and the reliability of the measurements of two of the best 2-D, transonic AWTSs: the NASA 0.3-m TCT and the ONERA T-2, and one of the most advanced conventional tunnels of the western world, the NAE 5'x5' wind tunnel in Ottawa. For the purpose of this study we will refer to these tunnels as the NASA, ONERA, and NAE tunnels. The report will develop along three main directives:

1. Description of the technical features and the related operating capabilities of the three wind tunnels.

2. Description and comparison of the wall adaptation strategies for the NASA and ONERA AWTSs and a description of the post-test analytical correction method for the NAE tunnel.

3. Comparison and validation of the measurements, made in the three tunnels on the CAST 10-2/DOA-2 airfoil, in transonic, high Reynolds number flows. We will refer to this airfoil as CAST 10.

The last part of this report is still today the subject of a cooperative, international program between NASA, NAE, ONERA, and DFVLR to assess methods to alleviate the wall interference effects in transonic flows.

2. PRINCIPLE OF WALL STREAMLINING

The basic working principle of an AWTS is to eliminate the wall interference at its source by adjusting the test section boundaries (Ref. 2, 5, 6, 7). This concept involves the shaping (streamlining) of the test section boundary,S, (at or near the test section wall) to a free air streamtube that encloses the model for each test condition. The shaping of the far field tunnel boundary cancels the wall aerodynamic interferences.

The boundary S splits the flow field into two parts:

1. The real flow field inside the boundary S.

2. An *imaginary*, irrotational flow field, extending from the boundary S to infinity.

The boundary S has to be located away from the model in order to avoid considering the viscous effects and, at the same time, to attenuate the model perturbation. The imaginary flow field is computed by the small

perturbation theory relative to the wall.

The general streamlining principle relies on matching on S two independent aerodynamic variables p and q in the real (p_r, q_r) and imaginary flow field (p_f, q_f). The variables p_r and q_r (that is, the components u_r and v_r of the perturbation velocity) are measured on S. One of them (for example, q_r) is used as a boundary condition to compute p_f on S. The streamlining of the boundary S is achieved if p_f and p_r are equal within a convergence criterion ϵ. The deformation of the boundary S influences, at the same time, both the real and the imaginary flow field. The matching of the imaginary and real flow field is complex and necessarily iterative. The streamlining procedure follows the flow chart on figure 1. The remarkable feature of the adaptation procedure is that the wall shaping can be determined without computing the flow field about the model.

The streamlining or adaptation procedure is simpler for 2-D flow fields where only two 2-D control surfaces are needed to control the boundary shape. The flow field is broken into three parts: the real part, which contains the model, and two imaginary parts. One imaginary part is above and the other is below the test section. Figure 2 explains graphically this concept.

The streamlining principle has been shown to be feasible with two different approaches: i) ventilated (perforated and/or slotted) wall test section and ii) impermeable, flexible walled test section. In the first approach, the control boundary S is inside the test section. The streamlining is fulfilled by modifying the velocity vector on the boundary S. Sucking or blowing, as appropriate, through the porous ceiling and floor control the velocity vectors on S. In the second approach, the control boundary S coincides physically with the ceiling and the floor (neglecting the wall boundary layer). The walls are streamlined by simply controlling the wall shape by a system of jacks.

3. COMPARISON OF THE NASA 0.3-m TCT AND THE ONERA T-2 TUNNEL

3.1 Physical Characteristics

3.1.1 Tunnel Circuit

The NASA 0.3-m TCT (Ref. 8, 9) and ONERA T-2 (Ref. 7, 10, 11, 12, 13) wind tunnel were designed to provide adequate Reynolds number and Mach number to simulate the design flight conditions of the current transonic transportation aircraft. Both tunnels are closed circuit, pressurized, and cryogenic. The Mach number operating range is about $0.1 < M_{\infty} < 0.95$ for the NASA tunnel and $0.3 < M_{\infty} < 1.1$ for the ONERA tunnel. The operating range in terms of Reynolds number per meter (at T = 120 K) is about $10^7 < R_m < 3 \times 10^8$ for the NASA tunnel and $3 \times 10^7 < R_m < 3 \times 10^8$ for the ONERA tunnel.

The circuits of the NASA and ONERA tunnels are about 28m and 25m long, respectively. We show the schematics of the tunnels in figure 3 and the operating envelope diagrams of the NASA (Ref. 14) and ONERA (Ref. 11) tunnel in figure 4. The data shown in the diagrams are related to empty test section.

The most important difference is in the working of the circuits. The ONERA tunnel is intermittent and the flow is produced by induction. Air is pressurized by a compressor in a $45m^3$ reservoir to a maximum pressure of 80 bars. The velocity is regulated by adjusting the area of the throat downstream of the test section (see figure 5). The NASA 0.3-m TCT is a continuous flow fan-driven tunnel which uses gaseous nitrogen (GN_2) as the test gas. The fan speed, and therefore the gas velocity and the Mach number, is automatically controlled by a computer. The liquid nitrogen (LN_2) used to cool the tunnel is sprayed into the tunnel circuit

downstream of the test section.

The short duration (90 to 120 seconds in transonic regime (Ref. 13)) of the runs, in T-2 causes some difficulties in making accurate tests. It causes problems with i) the control of the flow parameters, ii) the wall adaptation process, iii) the data acquisition, and iv) the surface temperature of the model and the test section walls. In its original configuration, a typical run of the ONERA tunnel developed along the following steps:

1) Starting the flow at low pressure (P = 1.1 bar) and low Mach number (M_∞ = 0.3), but at the right temperature.

2) Introducing rapidly the model into the stream. An auxiliary facility pre-cools the model to obtain a thermal equilibrium between the model and the flow.

3) Achieving the selected Mach number.

4) Adapting the walls.

5) Probing the wake and the pressure distribution on the model.

A complete test requires typically two runs. The first run (steps 1 through 4) is to adapt the walls and the second run (step 5) is to probe the wake (Ref. 7).

The injection flow feature allows the ONERA tunnel to achieve a lower turbulence level in the test section than the NASA tunnel. The turbulence, measured in the empty test section at T = 120 K and $M_\infty \approx 0.8$, is about 0.0015 and about 0.011 for the ONERA (Ref. 10, 15) and NASA (Ref. 16) tunnel, respectively. The turbulence level is defined as the root mean square of the pressure coefficient fluctuation.

3.1.2 Test Section

We show the schematics of the NASA and ONERA test sections in figure 5 and summarize the related physical and operating characteristics in Table I.

The dimensions in centimeters (Length x Height x Width) of the NASA and ONERA test sections are 185 x 33 x 33 and 132 x 37 x 39, respectively. The height and the width of both test sections are related to the entrance of the test sections. The flexible walls of both tunnels are made from special steel: 304 stainless steel for the NASA tunnel and INVAR steel for the ONERA tunnel. The walls must remain flexible down to cryogenic temperatures ($\approx$ 100 K). The wall thickness of the NASA test section varies along the wall length. The walls are less thick in the area close to the model. This is where the maximum wall curvature occurs. The wall thickness is: i) 0.32 cm from the entrance to the jack #6 and from the jack #17 to the exit, ii) 0.16 cm between the jacks #6 and #17. The wall thickness of the ONERA test section is constant (0.13 cm) along the entire length. The walls of the NASA test section (Ref. 8) are fixed: i) vertically and longitudinally at the upstream of the test section and ii) only vertically downstream. The walls can translate longitudinally as the wall shape changes. The downstream extremities of the walls of the ONERA test section are free in the vertical movement. Two moving flaps adapt the connection between the test section and the diffuser as the walls are deformed.

The first 18 jacks of the NASA test section are active. The jacks #19, #20, and #21 are not used in the streamlining process. These jacks are used only to smooth the connection between the streamlining position

4

and the diffuser. The connection is fulfilled on the basis of a prefixed criterion by starting from the position of the jack #18 (Ref. 17); thus the *aerodynamic length* of the test section is reduced to 142 cm. The first three jacks (#1, #2, #3) and the last jack (#16) of the ONERA tunnel participate in the streamlining process only in a passive way. The movement of these end jacks is calculated from an extrapolation of the wall adaptation strategy beyond the active jacks #4 through #15. The aerodynamic length of the test section is about 83 cm (Ref. 18). No pressure information is used upstream of the point X_L and downstream of the point X_U (see figure 5). The points X_L and X_U are located along the tunnel axis at a distance of 1.1 H (40.7 cm) upstream and downstream of the turntable center, respectively (Ref. 12). *H* is the test section height. The greater length of the flexible walls upstream of the model in the NASA tunnel should: i) guarantee a more precise definition of the undisturbed flow conditions and ii) reduce the source of error in obtaining interference free flow. This is linked to the finite length of the adjustable walls. The larger number of jacks also should guarantee a better wall adaptation.

The actuators deforming the walls of the ONERA and NASA tunnels are respectively hydraulic and screw jacks. All of them are controlled by electric stepper motors. For each tunnel the movement is transmitted by the jacks to the walls through a system of pull/push rods. Each actuator acts evenly on two points of the same rod. The local bending radius of the walls in both tunnels is checked before setting the new wall shape. The check is necessary to avoid exceeding the mechanical limit of the wall material. The two kinds of actuators are characterized by different features. The setting of the hydraulic jacks is faster but less fine than the screw jacks. Typically, in their current configuration:

1) The minimum jack displacement of the ONERA test section is 0.02 cm and the displacement speed is 0.6 cm/s.

2) The minimum jack displacement of the NASA test section is 0.01 cm and its displacement speed is 0.024 cm/s.

The jack displacement transducers of the NASA and ONERA tunnels are linear variable differential transformers and potentiometric comparators, respectively. The accuracy of the systems is ±0.013 cm and ±0.005 cm, respectively. The maximum movement of the jacks of the NASA test section is 7.62 cm upward and 2.54 cm downward. The maximum movement of the jacks of the ONERA test section is 2.5 cm both upward and downward. The larger wall/jack movement gives the NASA tunnel an adaptation capability at more severe operating conditions: that is, higher angle of attack, higher Mach number, and larger test model.

3.1.3 Pressure Measurement

Both tunnels are equipped to measure static pressure on the model and on the test section walls, and total pressure in the wake downstream of the model. Each flexible wall of the ONERA tunnel has 104 pressure holes (Ref. 13); 58 are drilled near the centerline and 23 on each side. The last ones are used to make measurements in 3-D tests. The pressure holes are more closely spaced in the model area. Each flexible wall of the NASA tunnel has 18 pressure taps along the centerline of the flexible walls at the same longitudinal position as the active jacks. The wake rake of the NASA tunnel is formed by 6 probes traversing the semispan of the test section. The system can translate vertically about 25.4 cm. It can be located at three different positions downstream of the turntable center: 31.8 cm, and 44.5 cm, 57.2 cm (Ref. 8). The wake rake of the ONERA tunnel consists of one probe located at the centerline of the test section. The original papers (Ref. 7, 10, 11, 12, 13) do not specify the position downstream of the model or the vertical movement of the wake rake. NASA and ONERA facilities use, in the pressure acquisition process, ten and seven 48-port scanning pressure valves, respectively. The pressure taps of the model and the wake rake in the NASA tunnel are linked directly

to individual pressure transducers.

The pressure transducers in the NASA tunnel are capacitive type (Barocell). The transducers are mounted on thermostatically controlled heater bases to maintain a constant working temperature. The transducers used to measure the pressure on the model and on the flexible walls work in the range ±6.9 bars. The transducers used to measure the pressure in the model wake work in the range ±1.4 bar. The average accuracy is ±1.5 mbar (Ref. 8). The pressure value is typically the average of 20 measurements. The pressure transducers in the ONERA facility are differential type (Kulite). The transducers are only thermally isolated but not thermostatically controlled; temperature corrections are necessary for these transducers (Ref. 12). The average accuracy of these transducers is ±2 mbars. The pressure value is typically the average of 80 measurements (Ref. 10).

3.1.4 Wind Tunnel Computer

Both tunnels are equipped with two communicating minicomputers to acquire and process the data and to manage the tunnel operations.

ONERA T-2 (Ref. 10):

HP21MX-F: to acquire and manage data both on the model and walls and to run the numerical program of the wall adaptation strategy.

HP21MX-E: to monitor and control the wind tunnel test conditions.

NASA 0.3-m TCT (Ref. 9, 17):

MODCOMP CLASSIC 7863 (CPU-A):   to acquire and manage wall data and run the numerical program of the wall adaptation strategy.

MODCOMP CLASSIC 7863 (CPU-B):   to acquire and manage model data and input and check the test conditions: that is, Mach number, Reynolds number, and angle of attack.

One MOTOROLA 6800 microprocessor controls the tunnel working parameters (temperature, pressure, and velocity).

3.1.5 Sidewall Boundary Layer Control System (BLC)

In 2-D tests, the model spans the test section from wall to wall; the sidewall BL makes a perfectly two-dimensional flow impossible. The sidewall BL also plays an important role in the aerodynamic interference. The effects due to the sidewall BL are particularly strong in transonic flows. In this situation, the boundary layer can separate from the sidewall, particularly where shock waves are present. This separation, in turn, introduces 3-D effects over the entire span of the model. Both test sections have a system to reduce the sidewall BL thickness. Both systems are still in development today.

The systems rely on the suction of the boundary layer through a porous plate. The suction region is located upstream of the model on each sidewall. Both the porous plates of the NASA (Ref. 8) and ONERA (Ref. 7) tunnels are located over the entire height of the test section. The length of the porous plate of the NASA tunnel is about 18 cm. The distance between the center line of the plate and the midpoint of the model

chord is 36 cm. The plate porosity is about 10 percent. The length of the plate of the ONERA tunnel is 18 cm. The distance between the center line of the plate and the midpoint of the model chord is 37.5 cm.

The NASA system is more powerful and versatile than the ONERA system. The NASA system, in fact, can work either in a passive or in an active mode (Ref. 19). The ONERA system can work only in a passive mode. The passive mode relies on the difference in pressure between the test section and the atmosphere. This system suffers from the following limitations:

1) The static pressure in the test section must be higher than the ambient pressure.

2) The maximum mass removal is limited by the LN_2 injected to maintain steady operating conditions. The active mode overcomes these shortcomings. The gas is removed by a re-circulation system using a cryogenic centrifugal compressor. The re-circulation system re-injects the gas into the tunnel at the high-speed diffuser. The sucked mass is controlled, in both modes, by digital valves. The selected mass flow removal rate is input to the microprocessor that controls the digital valves. The microprocessor also controls the compressor motor speed and the gas temperature at the compressor inlet.

3.2 Adaptation Strategies

Even though the NASA and the ONERA adaptation streamlining strategies rely on the same theoretical principle, the computations are quite different. Both strategies predict the ceiling and floor streamlining shapes. These shapes are set in the walls by a system of jacks. We will describe here the most important features of each strategy and then we will compare some operating aspects.

3.2.1 NASA 0.3-m TCT

Goodyer, Judd, and Wolf (Ref. 5, 6, 17, 20) developed the basic formula of the NASA strategy. The formula is related to one isolated flat wall in incompressible flow. The adaptation process is theoretically *one step*. The NASA strategy predicts the wall movement for streamlining by representing the physical wall with a vortex sheet. The local vortex intensity, at the streamwise jack position X, is given by the local aerodynamic loading:

$$\gamma(X) = V_r(X) - V_f(X) \tag{1}$$

where $V_f(X)$ and $V_r(X)$ are the local velocities, parallel to the wall, of the imaginary and real flow field, respectively. The strategy considers the vortex sheet as a flat plane (see figure 6) and approximates the computation of $\gamma(X)$ by:

$$\gamma(X) = u_r(X) - u_f(X) \tag{2}$$

The strategy computes the velocity normal component to the flat plane, induced by the vortex sheet, by the potential flow equation for vortex induced velocity:

$$v_f(\xi) = \frac{1}{2\pi} \int_{-\infty}^{+\infty} \frac{\gamma(X)}{(\xi - X)} dX \tag{3}$$

This perturbation velocity normal to the wall is balanced by a component of the wall velocity of the real flow

field. The balancing component is obtained by modifying locally the slope of the wall. This change in slope is computed by:

$$\frac{d}{dx} \Delta Z(\xi) = -\frac{v_f(\xi)}{U_\infty} = -\frac{1}{2\pi U_\infty} \int_{-\infty}^{+\infty} \frac{\gamma(X)\, dX}{(\xi - X)}$$

(4)

Equation 4 is integrated along the wall to obtain the *aerodynamic* movement ΔZ at position ξ. The strategy approximates the theoretical integration extremes $-\infty$, $+\infty$ with the points X_B and X_E, respectively (Ref. 20). These are located on both the flexible walls approximately at the beginning and the end of the test section, respectively (see figure 5). Finally the strategy interpolates the aerodynamic movement at the jack position X from $\Delta Z(\xi)$.

When two walls are considered in the same streamlining process, the simple use of equation 4 for each wall is inadequate, because of the strong aerodynamic interaction between the two flexible walls. The strategy considers this effect by using a coupling factor CF. This takes into account the effect of one wall on the adaptation of the other:

$$\Delta Z'_C(X) = \Delta Z_C(X) + CF\, \Delta Z_F(X)$$

(5.a)

$$\Delta Z'_F(X) = \Delta Z_F(X) + CF\, \Delta Z_C(X)$$

(5.b)

where the subscripts C and F refer to the ceiling and the floor, respectively. Since $\Delta Z'(X)$ tends to overshoot, the strategy uses a scaling factor SF to improve the convergence rate. The actual wall/jack movement is computed by:

$$\Delta Z_{wC}(X) = SF\, (\Delta Z_C(X) + CF\, \Delta Z_F(X))$$

(6.a)

$$\Delta Z_{wF}(X) = SF\, (\Delta Z_F(X) + CF\, \Delta Z_C(X))$$

(6.b)

Goodyer and Wolf evaluated experimentally the numerical values of both the coupling and the scaling factors to give satisfactory convergence (Ref. 5, 6). These values are the same for both the ceiling and the floor (CF = 0.35, SF = 0.8).

The aerodynamic interaction between the flexible walls also involves a change of flow at the model. This change necessitates an iterative procedure. The strategy computes, for each iteration step I:

1) the new wall/jack positions at X for the next iteration by:

$$Z_{wC,F}^{I+1}(X) = Z_{wC,F}^{I}(X) + \Delta Z_{wC,F}(X)$$

(7)

2) the component u of the velocity in the imaginary flow field over the new wall position as an average between those creating the vorticity:

$$u_f(X)^{I+1} = \frac{u_r(X)^I + u_f(X)^I}{2}$$

(8)

The velocity of the imaginary flow field is proportional to the jack movement. The velocity, computed by equation 8, can be corrected by formulas similar to equations 6.a and 6.b to consider the interference of the

other wall:

$$u_{fC}(X)^{I+1} = SF\,(u_{fC}(X)^{I+1} + CF\,u_{fF}(X)^{I+1})$$ (9.a)

$$u_{fF}(X)^{I+1} = SF\,(u_{fF}(X)^{I+1} + CF\,u_{fC}(X)^{I+1})$$ (9.b)

The strategy also applies to compressible flows. The compressible effects are considered by scaling the measured pressure coefficient to the incompressible value by:

$$C_{pi} = \beta\,C_{pc}$$ (10)

β is the Prandtl-Glauert coefficient: $(\beta = \sqrt{1 - M_\infty{}^2})$. The velocity component u_r is then computed from C_{pi} before use in the strategy computation.

3.2.2 ONERA T-2

Chevallier, Mignosi et al. (Ref. 7, 12, 13) developed the ONERA adaptation strategy. This strategy relies on a linearized theory and applies to one isolated, straight wall in incompressible flow. The strategy matches the real and the imaginary flow fields along two fictitious, horizontal flat control planes Σ_C and Σ_F. These are chosen near the ceiling and the floor of the test section, respectively. The strategy computes:

1) The normal (v_r) and the tangential (u_r) component on each plane $\Sigma_{C,F}$. These components are the projections of the measured velocity on the ceiling and the floor onto the normal and parallel directions to Σ_C and Σ_F, respectively.

2) The normal (v_f) and the tangential (u_f) component on each plane $\Sigma_{C,F}$ of the imaginary flow field. These components are computed by the Inverse Green Transform (IGT) and the Direct Green Transform (DGT) of the component u_r and v_r, respectively:

$$(IGT) \qquad v_f(X) = \frac{\beta}{\pi}\int_{-\infty}^{+\infty} \frac{u_r(\varsigma)\,d\varsigma}{(\varsigma-X)}$$ (11.a)

$$(DGT) \qquad u_f(X) = \frac{1}{\beta\pi}\int_{-\infty}^{+\infty} \frac{v_r(\varsigma)\,d\varsigma}{(\varsigma-X)}$$ (11.b)

The strategy approximates the integration limits $\pm\infty$ with $\pm 100\,H$ ($\pm 3.7\times10^3$ cm) with respect to the turntable center. The strategy breaks down the interval $[-\infty, +\infty]$ in three parts: $[-\infty, X_L]$, $[X_L, X_U]$, $[X_U, +\infty]$. It integrates equations 11.a and 11.b in the interval:

1) $[X_L, X_U]$ by using the projections onto Σ_C and Σ_F of the measured velocity on the ceiling and the floor, respectively.

2) $[-\infty, X_L]$ and $[X_U, +\infty]$ by using an estimation of the components u_r, v_r.
   The strategy estimates the components u_r, v_r outside the interval $[X_L, X_U]$ by representing the model by segments. Each segment has a uniform distribution of singularities: vortex, source, doublet, and vortex doublet. The strengths of each singularity are adjusted to match the velocity measured on the ceiling and the floor at the points X_L, X_U (Ref. 12).

The strategy weighs the u and v components in the real and imaginary flow field to get an average value u_f^P, v_f^P. The components of both the real and imaginary velocity are broken down into four contributions by a linear transformation. Unfortunately, the original papers (Ref. 7, 13) do not provide enough information to understand the meaning of the four contributions. The strategy computes a weighing factor ω for each contribution and weighs the corresponding velocity. The four contributions of the u component, for instance, read:

$$u_{1f}^P = u_{1f}\,\omega_1 + u_{1r}\,(1-\omega_1)$$

$$\dots\dots\dots\dots\dots\dots\dots\dots\dots\dots\dots$$

$$\dots\dots\dots\dots\dots\dots\dots\dots\dots\dots\dots$$ (12)

$$u_{4f}^P = u_{1f}\,\omega_4 + u_{4r}\,(1-\omega_4)$$

The inverse transformation is applied to calculate u_f^P and v_f^P. The strategy projects u_f^P and v_f^P onto the walls to create $u_f^{w'}, v_f^{w'}$. It computes the aerodynamic movement of the wall by the formula:

$$\Delta Z_{C,F}(X) = \int_{X_B}^{X} \frac{v_f^{w'}(\varsigma)}{(U_\infty + u_f^{w'}(\varsigma))}\, d\varsigma$$ (13)

for each jack location X.

The strategy computes the components $v_f^{w'}$ and $u_f^{w'}$ by the potential equation (Ref. 7):

1) The $v_f^{w'}$ component:

By integrating the equation:

$$\beta^2 \frac{\partial u}{\partial X} + \frac{\partial v}{\partial Z} = 0$$ (14)

with respect to Z, between Σ and the wall, the strategy obtains:

$$v_f^{w'} = v_f^P - \beta^2 \frac{\partial}{\partial X}\, u_f^P\, \Delta Z_\Sigma$$ (15)

where ΔZ_Σ is the actual distance between Σ and the wall.

2) The $u_f^{w'}$ component:

The irrotational flow field condition:

$$\frac{\partial^2 \varphi}{\partial X \partial Z} = \frac{\partial^2 \varphi}{\partial Z \partial X}$$ (16)

can be similarly written as:

$$\frac{\partial u}{\partial Z} = \frac{\partial v}{\partial X}$$ (17)

10

The strategy obtains, by integrating equation 17 with respect to Z between Σ and the wall:

$$u_f^{w'} = u_f^P + \frac{\partial}{\partial X} v_f^P \, \Delta Z_\Sigma \tag{18}$$

The strategy computes the derivative $\partial u_f^P / \partial X$ and $\partial v_f^P / \partial X$ as the slope of a least square curve, fitting the component u_f^P and v_f^P along $\Sigma_{C,F}$. Both the derivatives are assumed constant along ΔZ_Σ.

The strategy (Ref. 13) computes U_∞ at each iteration step far upstream of the test section by integrating on both Σ_C and Σ_F the equation:

$$\int_{-\infty}^{+\infty} [U(\zeta) - (U_\infty + u_f^P(\zeta))] \, Q(\zeta) \, d\zeta = 0 \tag{19}$$

where:
$U(\zeta)$ is the velocity along the tunnel axis,
$Q(\zeta) = 1/\cosh(\pi\zeta/\beta H)$ is a weighing function. $Q(\zeta)$ weighs heavily the points near the airfoil and decreases very rapidly as ζ moves away from the airfoil.

The strategy computes the actual wall movement by also taking into account the BL displacement thickness both on the flexible walls ($\delta^*_{C,F}$) and sidewalls (δ^*_{sw}). This is computed by an undefined integral technique (Ref. 7, 13). This technique considers the flexible walls like flat plates and uses the measured velocity distribution. Finally, the strategy computes the actual jack/wall movement, with respect to the flat wall position, by:

$$\Delta Z_{wC,F}(X) = \Delta Z_{C,F}(X) + \delta^*_{C,F}(X) + \delta^*_{sw}(X) \tag{20}$$

The flow chart in figure 7 summarizes the ONERA strategy.

3.2.3 Comparison of the NASA and ONERA Adaptation Strategies

The ONERA strategy relies on a more sophisticated and rigorous theory. The strategy considers the actual shape of the walls and the numerical values of the integration limits better approximate the theoretical values $+\infty$. Wolf (Ref. 5) assessed the streamlining errors on the NASA test section, related both to the finite length of the integration interval and to the hypothesis of flat vortex sheet, and found them to be very small. A conservative estimate of the error, related to the hypothesis of flat vortex sheet, on the velocity component u_f is given by:

$$\Delta u_f / U_\infty = -0.5 \, (\text{max. wall slope})^2 \tag{21}$$

This leads, even at high lift coefficient ($C_l = 5$) and by using a shallow test section, to an error in estimating the interference effect on C_l of less than 2 percent.

The ONERA strategy is much more complex from the computational point of view:

1) The ONERA strategy achieves numerically the aerodynamic coupling between the ceiling and

the floor by integrating equations 11.a and 11.b at the same time over the planes Σ_C and Σ_F. The NASA strategy aerodynamically couples the walls by experimental coefficients.

2) The ONERA strategy relies, for the computation of the wall/jack movement, on the weighing coefficients ω_j, $j = 1,..,4$. These coefficients can be very critical for the convergence rate like the scaling factors in the NASA strategy.

3) The ONERA strategy computes the free stream velocity U_∞. The NASA strategy operates with the measured free stream velocity. The computation of the free stream velocity is, indeed, necessary in the ONERA tunnel. The relatively short aerodynamic length of the test section does not allow accurate free stream measurements.

4) The ONERA strategy computes the boundary layer displacement thickness along the flexible walls and the sidewalls. The NASA strategy does not need to compute this parameter. It assumes the change in $\delta^*_{C,F}$ and δ^*_{sw}, due to the model, is small (as shown next).

Both the strategies can start from an *ad hoc* initial wall shape to accelerate the convergence process. The strategies can: i) compute the initial wall shape from a singularity representation of the tested model and/or ii) retrieve it from a previous test. The NASA strategy can retrieve the initial wall shape either:

1) from a data base. The wall shape is selected by assigning the actual test conditions: that is, the angle of attack, the Mach number, and the Reynolds number, or

2) from the aerodynamically straight wall shape. This wall shape considers the effects of the BL displacement thickness on the four walls. It achieves a nearly constant velocity distribution along the tunnel axis:

$$U(X) = U_\infty \tag{22}$$

Wolf (Ref. 17, 21) determined four aerodynamically straight contours, each corresponding to the following Mach number intervals: up to 0.5, from 0.5 to 0.75, from 0.75 to 0.85, and above 0.85. He did not consider the effect of Reynolds number. He found that the effect of Reynolds number on the aerodynamically straight wall shape are negligible with respect to the Mach number effects. He fixed intuitively the aerodynamically straight contours because the contours obtained experimentally displayed excessive waviness.

The convergence criterion of the NASA strategy is safer and more efficient. It guarantees a more direct evaluation of the wall adaptation quality. The iterative process of the ONERA strategy stops when the number of iterations, I, reaches the pre-selected value, N. The progress of the wall adaptation is assessed by checking, at successive iterations the distribution of: i) the wall shapes, ii) the Mach number at the walls, and iii) the pressure on the model. Archambaud (Ref. 13) says that usually the wall is considered to be adapted if the change of the wall position at each jack location is less than 0.01 cm. If this criterion is fulfilled, the other two are also satisfied. The adaptation process is repeated to satisfy the convergence criteria.

The iterations of the NASA strategy stop when the modulus of four errors in wall streamlining are simultaneously below prefixed values (shown in parenthesis):

1) the average of the imbalance in the pressure coefficients, at each jack position, between the real and imaginary flow field both on the ceiling and the floor (0.01),

2) the average induced pressure along the model chord (0.007),

3) the induced camber of the model (0.07 deg),

4) the induced angle of attack at the model leading edge (0.015 deg).

Due to the use of hydraulic jacks the overall ONERA adaptation process is much faster than the NASA process. One iteration of the ONERA and NASA process typically takes 7 seconds (Ref. 12) and 41 seconds (Ref. 21), respectively, according to the following table:

	ONERA	NASA
Data Acquisition	5 sec	10 sec
Adaptation Software	2 sec	1 sec
Wall Setting	0.2 sec	30 sec

The NASA process typically converges in 2-3 iteration steps. The pre-selected number of iterations of the ONERA process is usually 4-5. The effects of these strategies on the model data are discussed in section 6.2.3.

4. NAE 5'x5' WIND TUNNEL

4.1 Physical Characteristics

4.1.1 Tunnel Circuit

The NAE 5'x5' tunnel (Ref. 22, 23, 24, 25) is a modern, up-to-date large scale, high speed, blowdown tunnel. Both 2-D and 3-D tests can be made over a wide range of Mach numbers: $0.1 < M_\infty < 4.25$. Figure 8 shows the schematic of the tunnel.

The test gas is filtered, dried air. The air is compressed in a 1428 m^3 reservoir at the maximum pressure of 21 bars. The tunnel can independently set the Reynolds number and the Mach number. It can, in fact, independently control: 1) the temperature, 2) the density, and 3) the velocity.

1) A matrix of large thermal capacity tubes, set at the exit of the high pressure reservoir keep the gas temperature constant during the run.

2) A valve regulates the airflow from the reservoir into the setting chamber. The valve is controlled by a fully automatic electro-hydraulic system. It generates a constant stagnation pressure and therefore a constant gas density during the run. The control system can keep the stagnation pressure within 0.5 percent of the set value over the entire range of blowing pressure (1.2-15 bars). Baffles and screens reduce the noise and the turbulence level in the settling chamber.

3) A 2-D, about 15 m long nozzle accelerates the gas. The ceiling and the floor of the nozzle are flexible and are deformed by a system of 22 jacks per wall. This system of jacks is necessary in supersonic flow to shape the walls to the best contour for the selected Mach number.

13

The adjustment of the velocity in subsonic and transonic 2-D flow is achieved by: i) setting the walls of the nozzle parallel and ii) changing the ratio of the area of the diffuser second throat and the test section. This regulation is made using a servo-controlled hydraulic circuit. This is controlled by a microprocessor, dedicated to the control of the Mach number. The accuracy in setting and keeping the Mach number is ±0.002 (Ref. 23).

The intermittent working of the tunnel limits the test time. This is a function of the stagnation pressure. We plotted in figure 9 the estimated Reynolds number per meter and the test time (Ref. 22) as a function of the stagnation pressure at $M_\infty = 0.75$. The test time, shown in the figure also takes into account the time (about 2 seconds) necessary to establish a steady state flow inside the tunnel.

4.1.2 Test Section

The test section in the subsonic ($0.1 < M_\infty < 0.70$) and supersonic ($1.4 < M_\infty < 4.25$) regime is formed by the downstream end of the flexible nozzle. The ceiling and the floor are almost parallel in that part of the nozzle. Tests at transonic speeds ($0.7 < M_\infty < 1.4$) are achieved in an *ad hoc* test section. This can easily be included in tandem between the flexible nozzle and the variable diffuser. The turbulence level measured in this test section at $M_\infty = 0.8$ is 0.007 (Ref. 25). The turbulence level is defined as the root mean square of the pressure coefficient fluctuation.

The ceiling and floor of the transonic test section are perforated. The geometrical porosity is 21 percent. A fine mesh covers the perforated walls to eliminate the edge tone, generated by the perforation; the actual porosity is about 8.4%. The test section is provided with a passive BLC for 2-D tests. The suction area (61 cm x 46 cm) is located in the vicinity of the model and is covered by a porous plate with high flow resistance. This allows the system to perform a nearly uniform suction over the whole area. The system operates at a chosen suction velocity: $V_s = 0.85\% \ U_\infty$ (Ref. 24, 25).

The tunnel uses, in the pressure acquisition process, four 48-port scanning valves: 2 for the model and 1 for the ceiling and the floor. The pressure transducer is a quartz crystal oscillator with a nominal frequency of about 40 kHz. The resolution is 0.13 mbar. The transducer is mounted on a temperature controlled, thermally isolated base to get the maximum stability. The pressure value is the average of 100 measurements. The wake rake has four pressure probes traversing the semispan of the test section. The rake is located at 41 cm downstream of the model trailing edge. The rake can translate vertically 51 cm above the tunnel centerline and 25 cm below (Ref. 24, 25).

A DEC PDP 11/35 computer processes all the test activities (data acquisition, tunnel operation and control). A VAX 11/735 computer reduces and displays the data and also runs the wall interference correction program.

We summarize the more important features of the NAE transonic test section in Table II.

4.2 Interference Correction

Mokry and Ohman (Ref. 26, 27) developed the method to correct the wall interference in the NAE tunnel. This method applies to arbitrary 2-D test sections, including the ventilated test sections. It considers only the ceiling and the floor interference effects. The method computes the correction term to the streamwise induced velocity (that is, the correction term ΔM to the Mach number) and to the normal induced velocity (that is, the correction term $\Delta\alpha$ to the angle of attack). It relies on the measurement of:

14

1) the pressure distribution along the ceiling and the floor,

2) the model lift coefficient, and

3) the flow angle at a reference point far from the model.

The working hypothesis is that the flow field is correctable and sub-critical at the ceiling and floor. The relatively high value of the ratio H/c of the model-NAE tunnel system supports this hypothesis. The linearized equation of the potential:

$$\beta^2 \frac{\partial^2}{\partial x'^2} \varphi(x',y') + \frac{\partial^2}{\partial y'^2} \varphi(x',y') = 0 \tag{23}$$

describes the flow field in the inviscid part of the test section (unshaded area R inside the rectangle in figure 10). The origin of the axis system (x', y') is located at the quarter-chord of the airfoil. The potential of the disturbance velocity is decomposed in two parts:

$$\varphi(x',y') = \varphi_\infty(x',y') + \varphi_w(x',y') \tag{24}$$

where φ_s and φ_w are the potential of the perturbation due to the airfoil in free air and to the wall interference, respectively. The method computes φ_s as the principal part of the Laurent series expansion:

$$\varphi_\infty(x',y') = -\frac{\gamma}{2\pi} tg^{-1} \frac{\beta y'}{x'} + \frac{\mu}{2\pi\beta} \frac{x'}{[x'^2+\beta^2 y'^2]} \tag{25}$$

The first and the second term consider the disturbance of the lift and the displacement effect of the model, respectively. No wake effect (modeled by a source term) appears in equation 25. Mokry says this term is negligible up to the stall (Ref. 26). The method computes:

1) The strength of the vortex γ from the Joukowski theorem: $\gamma = 0.5cC_l$, where c is the model chord and C_l is the lift coefficient.

2) The strength of the doublet μ from: $\mu = c^2 A$, where A is the airfoil non-dimensional cross-section area.

As a next step we describe the computation of the wall interference potential φ_w. The wall interference potential fulfills equation 23:

$$\beta^2 \frac{\partial^2}{\partial x'^2} \varphi_w(x',y') + \frac{\partial^2}{\partial y'^2} \varphi_w(x',y') = 0 \tag{26}$$

By using the linear transformation:

$$\xi' = \frac{x' - x'_1}{\beta}, \quad \eta' = y' - y_1' \tag{27}$$

15

equation 26 is reduced to the Laplace equation:

$$\frac{\partial^2}{\partial \xi'^2} \varphi_w (\xi', \eta') + \frac{\partial^2}{\partial \eta'^2} \varphi_w (\xi', \eta') = 0 \tag{28}$$

By differentiating equation 28 with respect to ξ':

$$\frac{\partial}{\partial \xi'} \left[\frac{\partial^2}{\partial \xi'^2} \varphi_w(\xi', \eta') + \frac{\partial^2}{\partial \eta'^2} \varphi_w(\xi', \eta') \right] = 0 \tag{29}$$

and with the definition:

$$u_w(\xi', \eta') = \frac{\partial}{\partial \xi'} \varphi_w(\xi', \eta') \tag{30}$$

the method obtains:

$$\frac{\partial^2}{\partial \xi'^2} u_w(\xi', \eta') + \frac{\partial^2}{\partial \eta'^2} u_w(\xi', \eta') = 0 \tag{31}$$

The method integrates equation 31 by the Fast Fourier Transform. This computation is described in references 26 and 27. The boundary conditions along the sides $(x_1', y_2') - (x_2', y_2')$ and $(x_1', y_1') - (x_2', y_1')$ of the rectangle (see figure 10) are computed by:

$$u_w(\xi', \eta') = -\beta \left[0.5 \, F(x', y') + \frac{\partial}{\partial x'} \varphi_\infty(x', y') \right] \tag{32}$$

where $F(x', y')$ is a cubic spline function. It interpolates and smoothes the pressure coefficients measured on the ceiling and on the floor. No pressure measurement is available across the stream; the boundary condition along the sides $(x_1', y_2') - (x_1', y_1')$ and $(x_2', y_2') - (x_2', y_1')$ are computed by interpolating linearly the corner values. The streamwise induced velocity and the normal induced velocity are represented by the derivatives $u_w(0,0) = \partial \varphi_w(0,0)/\partial x'$ and $v_w(0,0) = \partial \varphi_w(0,0)/\partial y'$ at the airfoil quarter of the chord, respectively.

4.2.1 Mach Number Correction

The method (Ref. 26) computes the Mach number correction by differentiating the adiabatic relation between the velocity and the Mach number:

$$\Delta M = \left[1 + \frac{(k-1)}{2} M_\infty^2 \right] \frac{M_\infty}{\beta} u_w \left(-\frac{x_1'}{\beta}, -y_1' \right) \tag{33}$$

4.2.2 Angle of Attack Correction

The difficulty to apply the boundary conditions to the normal velocity component complicates the computation of $v_w(0,0)$ by the direct integration of equation 26. The method computes this component as the harmonic conjugate of u_w at the point $(0,0)$. Equation 28 can be written as:

$$\frac{\partial}{\partial \xi'} u_w(\xi',\eta') + \frac{\partial}{\partial \eta'} v_w(\xi',\eta') = 0 \tag{34}$$

The method computes $v_w(0,0)$ by integrating equation 34 with respect to η' between a reference point (x_o', y_o') and $(0,0)$:

$$v_w(0,0) - v_w(x'_o, y'_o) = -\int_{y_o'}^{0} \frac{\partial}{\partial \xi'} u_w(\xi',\eta') \, d\eta' \tag{35}$$

The method computes $v_w(x_o', y_o')$, with the definition $v_w = \partial \varphi_w / \partial y'$, by differentiating equation 24 with respect to y':

$$\frac{\partial}{\partial y'} \varphi(x_o', y_o') = \frac{\partial}{\partial y'} \varphi_\infty(x_o', y_o') + \frac{\partial}{\partial y'} \varphi_w(x_o', y_o') \tag{36}$$

If (x_o', y_o') is inside the linearized flow region:

$$\frac{\partial}{\partial y'} \varphi(x_o', y_o') = \psi(x_o', y_o') \tag{37}$$

where $\psi(x_o', y_o')$ is the flow angle at the reference point. This angle is usually measured by a laser velocimeter. Mokry suggests $\psi(x_o', y_o') = 0$ if the distance between the airfoil and the upstream side of the rectangle is large enough and:

$$C_p(x_1', y_1') \approx C_p(x_1', y_2') \approx 0 \tag{38}$$

From equation 36 and 37:

$$\frac{\partial}{\partial y'} \varphi_w(x_o', y_o') = \psi(x_o', y_o') - \frac{\partial}{\partial y'} \varphi_\infty(x_o', y_o') \tag{39}$$

The correction term to the angle of attack finally reads:

$$\Delta \alpha = -\int_{y_o'}^{0} \frac{\partial}{\partial \xi'} u_w(\xi',\eta') d\eta' + \psi(x_o', y_o') - \frac{\partial}{\partial y'} \varphi_\infty(x_o', y_o') \tag{40}$$

5. MODEL DESCRIPTION

We used the aerodynamic measurements on the CAST 10 airfoil to compare, on the operative background, the ONERA, NAE, and NASA processes. We show the sketch of the airfoil and the related geometrical and aerodynamic design characteristics in figure 11. CAST 10 is an unclassified, German airfoil, designed by DORNIER for academic purposes and to gain knowledge and experience on the super-critical airfoil technology.

The aerodynamic behavior of the CAST 10 airfoil is typical of the super-critical airfoils. The lift curve exhibits a linear part at low angles of attack and a non-linear part (super-lift region) before the flow breakdown region. We show in figure 12 an artistic illustration of the lift curve of a super-critical airfoil. During previous tests this airfoil was found to be extremely sensitive to changes in the Mach number, Reynolds number, and to the wall interference. Because of its high sensitivity to the wall interference, it is today considered an efficient tool to test the flow quality in wind tunnels (Ref. 28).

5.1 Airfoil Model

The tests, on which our analysis relies, were made using two different models of the CAST 10 airfoil. The models were built at ONERA and NAE, respectively. We will refer to the ONERA and NAE models as the French and Canadian models, respectively.

The French model has a chord of 18 cm. It is made from steel MARVAL 18 and is fitted with 103 pressure taps. The Canadian model has a chord of 22.9 cm. It is made from steel VASCOMAX 200 and is fitted with 80 pressure taps. The pressure taps on the French model are swept along the centerline. Of all the orifices on the Canadian model, 67 are staggered along the centerline, the others are located spanwise on each side of the centerline. The models were built according to the cryogenic specifications and the manufacturing accuracy is very high. The average deviation (Ref. 29) from the design conditions of the upper surface coordinates of the Canadian model is $\Delta z/c = 0.00058$. The average deviation of the coordinates of the upper surface between the NAE and ONERA model is $\Delta z/c = 0.0001$. The technicians of NASA LaRC checked both the models to assure that the aero-thermo-elastic effects did not spoil the model shape.

The tunnel set up for the two models differs because of the choice of the reference plane of the angle of attack. The reference plane of the French model links the leading and the trailing edge. The reference plane of the Canadian model links the mid-points between the upper and lower surface at $x/c = 0.194$ and $x/c = 0.639$. The geometrical angle between the two reference planes is 0.882 deg (Ref. 29).

The models were tested with both free and fixed transition on both the upper and lower airfoil surfaces. Transition was fixed on the Canadian model by using a carborundum strip located at 5 percent of the chord. The average grit size was 0.028 mm. Transition was fixed on the French model for the ONERA tests by using a carborundum strip located at 6 percent of the chord. The average grit size was 0.045 mm. Transition was fixed for the NASA tests by using a strip of glass beads located at 5 percent of the chord. The average bead size was 0.053 mm.

We show the geometrical parameters W/c and H/c of the model-wind tunnel systems in Table III.

6. ANALYSIS OF THE DATA

6.1 Evaluation of Secondary Effects

The comparison and the validation of the data from the NAE (Ref. 24, 25), the NASA (Ref. 30, 31, 32) and the ONERA (Ref. 33, 34) tunnels is mainly aimed at an evaluation of both the adaptation processes and Mokry's method in alleviating the ceiling and floor interference effects. We preliminarily examined the available experimental data. This was necessary to evaluate secondary effects and therefore to remove variables from the validation analysis. The nominal operating test conditions of both the preliminary analysis and the following

validation analysis are: $M_{\infty} = 0.765$, $R_c = 20 \times 10^6$. We show the actual test conditions on the related figures. The normal force coefficient and the drag coefficient from the NASA, NAE, and ONERA tunnels are computed by integrating the pressure distribution along the model surfaces and across the model wake, respectively. Further, additional force measurements from a balance are also available for the NAE tunnel. The low values of the angles of attack ($-3 < \alpha < 3$), according to the reference system of the French model, allowed us to approximate the lift coefficient with the normal force coefficient ($C_l \approx C_n$).

We considered the secondary effects linked to: i) the transition tripping, ii) the BLC suction velocity, and iii) the sidewall interference effects. We also preliminarily checked two sets of the corrected, aerodynamic coefficients C_l and C_d, from the NAE tunnel (Ref. 24). One set was obtained by the pressure integration. The other set was measured by an aerodynamic balance. The comparison showed only slight discrepancies. The root mean square deviation, we computed for the test case $M_{\infty} = 0.766$, $R_c = 20.2 \times 10^6$, in the range of the angle of attack ($-2 < \alpha < 2$) was 0.004 for C_l and 0.001 for C_d. The plots show the first set of data.

6.1.1 Transition Tripping

As expected artificially fixing transition showed only negligible effects on integral aerodynamic coefficients (C_l, C_d), at test Reynolds numbers (R_c) on the order of 20×10^6. We verified this by comparing the lift (see figure 13) and the drag curve (see figure 14) of the Canadian model from the NAE tunnel. The drag coefficients were computed from the pressure measured by the pitot of the wake rake, located at the center line of the test section. In order to quantify this check we computed the least square linear fit of the two sets of the lift coefficients in the range $-2 < \alpha < 2$. The curve intercept a and slope b of the two linear fits are the same up to the second decimal place (a = 0.33, b = 0.18).

6.1.2 BLC Suction Velocity

We found the BLC suction velocity does not strongly affect the lift curve up to the flow breakdown region. We verified this by comparing the lift curves of the Canadian model from the NASA tunnel (see figure 15). Murthy (Ref. 31) measured the C_l coefficients at the minimum ($V_s = 0$) and at the maximum ($V_s = 0.85\%$ U_{∞}) suction velocity. The parameters of the least square linear fit, in the range $-2.5 < \alpha < 1.5$, are the same up to the second decimal place (a = 0.35, b = 0.19).

We plotted the lift coefficients obtained by Mineck (Ref. 30) at $V_s = 0$ in the same figure to get a preliminary idea of the repeatability of the data from the NASA tunnel. The check turned out to be satisfactory up to the flow break region ($\alpha < 1.5$). We found only a slight discrepancy in the slope of the curve. The slope of the least square fit of Mineck's data is: b = 0.18. The drag curve (see figure 16) also shows a reasonable repeatability at low and moderate angles of attack ($\alpha < 1.5$).

6.1.3 Sidewall Interference Effect

Stanewsky (Ref. 28) found that the sidewall interference reduces the magnitude of the non-linearity feature of the lift curve in ventilated test sections. The reduction in ΔC_l is inversely proportional to the ratio W/c. We assumed Stanewsky's remark is true also for solid wall test sections.

We show in figure 17 the lift curves of the French (Ref. 32) and the Canadian (Ref. 30) model from the NASA tunnel. These lift curves correspond to the maximum (1.8) and the minimum (1.4) ratio W/c of the available experimental data. As expected:

1) The low values of the ratio W/c strongly affect the super-lift feature of the two models.

2) The reduction in ΔC_l is almost the same for the two models. The ratio W/c is almost the same for the two model-wind tunnel systems.

We quantified these effects by comparing, once again, the parameters of the least square linear fit. The reduction in ΔC_l, that is, the linearization of the lift curve, is quantified by the correlation coefficient r. This parameter is a measure of the fitting quality of the curve. It ranges in the interval $0 < r < 1$. The correlation coefficients for the the lift curve of the French and Canadian model in the range $-1.09 < \alpha < 1.85$ (according to the reference system of the French model) are 0.98 and 0.83, respectively. The intercept and the slope also are almost the same for the models: $a = 0.33, b = 0.17$ for the French model and $a = 0.35, b = 0.18$ for the Canadian model.

6.2 Validation and Comparison

6.2.1 General Remarks

The validation analysis is the technical tool to assess the flow quality in wind tunnels. The data are usually validated either from the comparison with interference free data, or from the evaluation of the residual interference.

The validation of the NASA, NAE, and ONERA data was particularly hard because we could not:

1) use experimental data from other tunnels as reference data. The tunnels of our concern are supposed to be among the best in the western world. The data of these tunnels are often used to validate the data from other tunnels.

2) compute by a common technique and then compare the residual interference. We considered the possibility of using the numerical program TWINTN4 WIAC (Ref. 35) to compute the residual interference in the three tunnels. The code is quite general and can be used both for flexible and ventilated walls test sections. The use of this program on a routine basis is somewhat difficult. Its use requires user intuition and intervention as well as substantial computing time.

We validated the experimental data from the comparison with the theoretical ones. These are computed by the most recent version (MCMJ-11) of the GRUMFOIL code (Ref. 36, 37). Bearing in mind the limitations involved by any numerical approach, the analysis gives only some indications of the experimental data quality.

6.2.2 GRUMFOIL Code

GRUMFOIL is a computer program for calculating the steady, viscous, transonic flow over two-dimensional airfoils. The solution relies on an iterative scheme of the strong interaction between the boundary layer and the inviscid flow field. The boundary layer is computed by integral entrainment methods. The inviscid flow field is computed by integrating, by a multigrid method, the full non-linear potential equations.

The use of GRUMFOIL for the present application suffers from the limitation that the code does not adequately deal with large separated flow regions. In this condition the iteration scheme loses some

effectiveness. The solution, when possible, can be obtained only by using very low relaxation factors with a remarkable increase in computer time. This shortcoming restricts the use of the code for small/moderate angles of attack and/or Mach numbers.

We run the code in the inverse mode such that the angle of attack is computed from the input lift coefficient. We always: i) input the code with the NASA test conditions: Mach number, Reynolds number, and lift coefficient, and ii) fixed the transition location between $x/c = 0.002$ and $x/c = 0.05$.

6.2.3 Results of the Validation Process

We made the validation analysis by comparing with the theoretical results:

1) local quantities such as the pressure distribution and the shock location on the model surface,

2) (as suggested by McCroskey (Ref. 38)), integral quantities such as the drag curve as a function of the Mach number, and the slope of the linear part of the lift curve as a function of the Reynolds number and the Mach number.

We also compared: 1) the NASA and NAE maximum lift coefficient as a function of the Reynolds number and Mach number, 2) the two-dimensionality of the flow in the test section of the NASA and NAE tunnel. Unfortunately, the above limitation of the GRUMFOIL code prohibits its effectiveness in determining C_{lmax}. The sparsity of the available data did not allow us to do the analysis on C_{lmax} for the ONERA data. The intermittent working of the ONERA tunnel makes it more difficult to do systematic tests in terms of Mach number, Reynolds number, and angle of attack.

6.2.4 Pressure Distribution

We show the pressure distribution on the French and Canadian model in figures 18 and 19, respectively. The agreement of the pressure coefficient of the NASA and NAE tests with the GRUMFOIL results is excellent. We can estimate the agreement of the NASA, ONERA, and GRUMFOIL pressure distribution reasonably good. Note that the NASA and the ONERA data were obtained with fixed and free transition, respectively. The mismatching of this test condition gives rise to the small discrepancy in the C_p coefficients on the model upper surface, even though the test Reynolds number is high enough ($R_c \approx 20x10^6$). The discrepancy starts from $x/c \approx 0.10$ and increases constantly up to $x/c \approx 0.70$. The tripping anticipates the increase of the displacement thickness. This gives rise, in turn, to an increase of the local velocity and therefore to a decrease of the local pressure.

We compared the pressure distributions on the French model also at other test conditions (see figure 20). As expected the better matching of the test conditions (both sets of data were obtained at free transition) involves a better agreement of the pressure distribution. The agreement is even more surprising because of the severity of the test conditions. The lift coefficient is very close to the maximum value ($C_{lmax} \approx 0.655$, see figures 13, 15 and 17). It is well known that the flow field is very sensitive to the wall interference near stall conditions. The severity of the test conditions discouraged us to attempt to run the GRUMFOIL code.

6.2.5 Shock Location

We used the classical criterion to determine the abscissa x_s/c of the shock wave on the model upper surface. This criterion locates the shock at the point where the slope of the pressure profile changes sign. We

computed this location as the abscissa of the cross-point of the curves, interpolating the pressure coefficients before and after the suction peak. Figure 21 explains graphically this criterion. We used the described criterion to locate the shock location from the GRUMFOIL pressure distribution. This was necessary to be consistent with the shock location from the experimental data.

We show in figures 22 and 23 the shock location as a function of the lift coefficient on the Canadian and French model, respectively. The agreement of both the experimental data and the GRUMFOIL results is excellent for the Canadian model. The root mean square deviation is 0.022 and 0.027 for the NASA and NAE data, respectively. The trends of the NASA and NAE data are also consistent with the stall. Because of the reason stated before, we could expect a disagreement of the shock location at higher lift coefficient. The agreement of the NASA data and the GRUMFOIL results is satisfactory for the French model. The root mean square deviation is 0.031. The trend of the NASA data is also consistent with the stall. The sparsity of the available data does not allow us to evaluate the ONERA data.

6.2.6 Drag Curve

We found the agreement between the NASA and NAE drag coefficients of the Canadian model is excellent over the whole range of Mach number, $0.70 < M_\infty < 0.79$ (see figure 24). Both sets of data show:

1) practically the same drag divergence Mach number. We could roughly include this value in the range: $0.765 < M_\infty < 0.775$.

2) the drag creep before the drag divergence. The drag creep is a typical phenomenon of some super-critical airfoils (Ref. 39). It is generated by a complicated interaction of several causes and is strongly related to the boundary layer condition and the airfoil fluid shape. The agreement of the experimental and theoretical results is also satisfactory up to $M_\infty = 0.765$.

The NASA drag coefficients of the French model are in good agreement with the theoretical results (see figure 25). Even though the numerical results are systematically higher than the experimental data, the curves show the same trend over the whole range of the computed results ($0.70 < M_\infty < 0.77$). The agreement of the ONERA drag coefficients with both the NASA and theoretical results is also reasonably good up to $M_\infty \approx 0.73$. The ONERA data are lower than the NASA data at higher Mach number ($M_\infty = 0.762$, $M_\infty = 0.765$). A shock weakening, due to a local decrease of the Mach number, could have produced the drop of the drag coefficients. The Mach number decrease, in turn, was probably due to stronger residual wall interferences. Unlike the drag curve of the Canadian model, both the NASA and ONERA data show no drag creep in the drag curve of the French model. The different test Reynolds number could explain the absence of this phenomenon.

6.2.7 Lift Curve Slope

We computed the slope of the linear part of the lift curve ($C_{l\alpha}$) by the finite difference of two adjacent lift coefficients:

$$C_{l\alpha} = \frac{C_{l1} - C_{l2}}{\alpha_1 - \alpha_2}$$

(41)

We show the NASA data with the experimental tolerance band. We computed the tolerance band from the

measurement accuracies of ±0.005 for the lift coefficient and ±0.01 deg for the angle of attack (Ref. 9).

We show the slope of the linear part of the lift curve for the Canadian model as a function of the Mach number and Reynolds number, in figures 26 and 27, respectively. To show quantitatively the benefits of the wall streamlining in reducing the wall interference effects, we plotted the uncorrected Canadian data in the same figure. The agreement of the NASA and NAE data and the theoretical results are reasonably good on the whole interval of the Mach number. Both the Canadian data and the theoretical results practically lie within the tolerance band of the NASA data. The adding of numerical approximation error in computing the finite difference slope could explain the slight wavering of the theoretical results. The agreement of the NASA and NAE data is excellent on the whole interval of the Reynolds number (see figure 27). We show in the figure only the GRUMFOIL results computed at R_c = $6x10^6$ and R_c = $20x10^6$. The lift curve slope computed at R_c = $10x10^6$ and R_c = $15x10^6$ turned out to be physically unacceptable, even though the runs were successful from the numerical point of view. The runs showed, in fact, good convergence process and the residual error dropped four orders of magnitude. A possible cause of convergence toward a wrong solution, at the selected test conditions (C_l, R_c, M_∞), could be due to the inability of the code to match the potential and viscous solution because of the presence of a large pressure gradient close to the leading edge.

We show the lift curve slope of the French model as a function of the Reynolds number on figure 28. The agreement of the NASA and the theoretical results are satisfactory in the trend. The discrepancy in $C_{l\alpha}$ arises because the GRUMFOIL code predicts the super-lift phenomenon, while the experiments, as shown before (see figure 17), do not show this feature. The experimental lift coefficients C_{l1} ($C_{l1} \approx 0.4$) used to compute $C_{l\alpha}$ from equation 41 are beyond the linear range for the GRUMFOIL code. This is easily verified from figure 29, where we show a typical experimental lift curve of the CAST 10 airfoil from the NASA tunnel and the corresponding theoretical curve. We shifted the theoretical curve along the α-axis to match the angle of attack at C_l = -0.019. The sparsity of the available data does not allow us to evaluate the ONERA data.

Maximum Lift Coefficient and Two-Dimensionality of the Flow Field

We assessed once again:

1) the good agreement of the NASA and NAE data by comparing C_{lmax} as a function of the Reynolds number (see figure 30) and the Mach number (see figure 31). The two sets of data show similar trends if we do not consider the anomalous lift coefficient at M_∞ = 0.8 from the NASA tunnel. The difference is perhaps due to the different operations of BLC. The NAE data were obtained with the suction velocity V_s = 0.85% U_∞ while the NASA data were obtained without BLC suction (V_s = 0). The matching of the results is even more surprising because the residual interference effects are opposite in sign in ventilated and in solid test section. The wall interference, in fact, increases the maximum lift coefficient in ventilated test section (Ref. 28) and decreases the maximum lift coefficient in solid wall test section (Ref. 21).

2) The wall streamlining improves the two-dimensional flow in the test section. We easily verified this by comparing the profile of the NASA and NAE drag coefficient along the transverse dimension of the test section. The drag profiles were obtained at $C_l \approx 0.3$ (see figure 32) and $C_l \approx 0.6$ (see figure 33), respectively. The NASA data are even more remarkable because: i) what obtained without BLC (V_s = 0), and ii) the wake rake of the NASA tunnel was located nearer to the trailing edge of the model (27.4 cm) (Ref. 30) than the wake rake of the Canadian tunnel (41 cm).

7. CONCLUDING REMARKS

We have compared critically three of the best 2-D, transonic wind tunnels of the western world: i) NASA 0.3-m TCT which is fitted with an AWTS, ii) ONERA T-2 which is also fitted with an AWTS, and iii) NAE 5'x5' which has a conventional, ventilated test section. We have discussed:

1) The general, technical features of the tunnel circuits and, in more detail, the operational and performance aspects of the test sections.

2) The correction techniques: two wall adaptation strategies and one classical correction method (Mokry's method).

3) Various sets of airfoil data. We validated these data by the comparison with the theoretical results of the GRUMFOIL code.

The data were obtained on two models of the CAST 10-2/DOA-2 supercritical airfoil. The high sensitivity to the changes of the Mach number and of the Reynolds number and, moreover, to the wall interference, makes this airfoil a useful tool to evaluate the flow quality in a wind tunnel.

We found the NASA and the NAE tunnel to have the same data accuracy. However, the NASA tunnel appears to have a better ratio of benefits to costs because:

1) the smaller dimensions of both the circuit and the tests section involve less initial investment, maintenance, and operation costs.

2) The operation of a cryogenic wind tunnel is cheaper and more effective for independent control of the Mach number and the Reynolds number.

3) The AWTS: i) allows immediate interference free measurements, without needing to use any post-test correction method and ii) improves the general flow characteristics in the test section as, for instance, the two-dimensionality of the flow field.

The above mentioned remarks are, from a general point of view, true also for the ONERA tunnel. The ONERA tunnel suffers, however, from the shortcoming of intermittent operation. This feature strongly limits the tunnel capability in performing systematic tests at severe flow conditions. This limitation did not allow us to: i) definitively validate the results because of a sparsity of available data and ii) obtain a precise insight into the capability of the wall adaptation process. In addition, the ONERA tunnel is not able to test at such high Reynolds numbers as routinely set in the NASA tunnel.

We can affirm, on the basis of the objective considerations in this report, that the NASA tunnel is more powerful and effective for 2-D, transonic tests up to full scale Reynolds numbers.

8. REFERENCES

1. Martindale, W. R.; Butler, R. W.; et al.: Study on Needs for a Magnetic Suspension System Operating with a Transonic Wind Tunnel. NASA CR 3900, May 1985.

2. Sears, W. R.; and Erickson, J. C.: Adaptive Wind Tunnel. Ann. Rev. Fluid Mech., Vol. 20, 1988.

3. Wolf, S. W. D.; and Kilgore, R. A.: Adaptive Wall Test Section. Lecture Series on: "Advanced Experimental Techniques for Transonic Wind Tunnel" presented at The National Defense Academy Department of Aeronautical Engineering, Yokosuka, Oct. 1987.

4. Ashill, P. R.; and Weeks, D. J.: A Method for Determining Wall Interference Corrections in Solid Wall Tunnel from Measurements of Static Pressure at the Walls. AGARD Conference Proceedings on: "Wall Interference in Wind Tunnel", N.335, Paper N.1, London, May 1982.

5. Wolf, S. W. D.: The Design and Operational Development of Self Streamlining Two-Dimensional Flexible Walled Test Sections; NASA CR 172328, Mar. 1984.

6. Wolf, S. W. D.; and Goodyer, M. J.: Predictive Strategy for Two-Dimensional Flexible Walled Adaptive Wind Tunnel. A detailed Description of the First One-Step Method. AASU Memo 85/12, Jan. 1986.

7. Chevallier, J. P.; and Mignosi, A.; et al.: T-2 Wind Tunnel Adaptive Walls: Design, Construction and Some Typical Results. La Recherche Aerospatiale (English Edition), N.4, Jul./Aug. 1983, pp 1-19.

8. Ladson, C. L.; and Ray, E. J.: Evolution and Operation Characteristics of Two-Dimensional Test Section of the Langley 0.3-m Transonic Cryogenic Tunnel. NASA TP 2749, Sept. 1987.

9. Design Library of the 0.3-m TCT Test Section, Experimental Techniques Branch, NASA LaRC, Hampton (VA)

10. Gobert, J. L.: Data Acquisition and Process Control in The Self-Correcting Cryogenic Wind-Tunnel T-2 at ONERA/CERT by Integration of Two Minicomputers. 11th International Congress on: "Instrumentation in Aerospace Simulation Facilities", Stanford, Aug. 1985.

11. Michel, R.; and Mignosi, A.: Adaptation and First Cryogenic Operation of T-2 ONERA/CERT Wind Tunnel. La Recherche Aerospatiale (English Edition), N.2, Mar./Apr. 1982, pp 75-85.

12. Archambaund, J. P.; Blanchard, A.; et al.: Instrumentation and Testing Techniques in T-2 Transonic Cryogenic Wind Tunnel at ONERA/CERT. 11th International Congress on: "Instrumentation in Aerospace Simulation Facilities", Stanford, Aug. 1985.

13. Archambaud, J. P.; and Mignosi, A.: Two-Dimensional and Three-Dimensional Adaptation at the T-2 Transonic Wind Tunnel of ONERA/CERT. AIAA 15th Aerodynamic Testing Conference, San Diego, May 1988.

14. Rallo, R. A.; Dress, D. A.; et al.: Operation Envelope Chart for The Langley 0.3-m Transonic Cryogenic Wind Tunnel. NASA TM 89008, Aug. 1986.

15. Dor, J. B.; Mignosi, A.; et al.: Qualification of the T-2 Wind Tunnel in Cryogenic Operation. B: Flow Fluctuation - Particle Detection and Qualification. NASA TM 77782, Dec. 1984.

16. Igoe, W. B.: Private Communication

17. Wolf, S. W. D.: Wall Adjustment Strategy Software for Use With the NASA Langley 0.3-m Transonic Cryogenic Tunnel Adaptive Test Section. NASA CR 181694, Nov. 1988.

18. Wolf, S. W. D.: Private Discussion

19. Johnson, C. B.; Murthy, A. V.; et al.: A Description of the Active and Passive Side Wall Boundary Layer Removal System of the 0.3-m Transonic Cryogenic Tunnel. NASA TM 87764, Nov. 1986.

20. Wolf, S. W. D.; and Goodyer, M. J.: Predictive Wall Adjustment Strategy for Two-Dimensional Flexible Walled Adaptive Wind Tunnel - A Detailed Description of the First One-Step Method. NASA CR 181635, Jan. 1988.

21. Wolf, S. W. D.: Evaluation of a Flexible Wall Testing Technique to Minimize Wall Interference in the NASA Langley 0.3-m Transonic Cryogenic Tunnel. AIAA 26th Aerospace Science Meeting, Reno, Jan. 1988.

22. Brown, D.: Information for Users of the National Research Council's 5'x5' Blowdown Wind Tunnel at the National Aeronautical Establishment. Laboratory Technical Report HA-6, Ottawa, Sept. 1977.

23. Ohman, L. H.; Brown, D.; et al.: Recent Improvements to the NAE 5'x5' Blowdown Wind Tunnel. N.A.E. Aeronautical Note N. 31, Ottawa, Aug. 1985.

24. Chan, Y. Y.: Wind Tunnel Investigation of CAST 10-2/DOA-2 12% Super-critical Airfoil Model. Laboratory Technical Report HA-162, Ottawa, May 1986.

25. Chan, Y. Y.: Wind Tunnel Investigation of CAST 10-2/DOA-2 12% Super-critical Airfoil Model, Phase II. Laboratory Technical Report HA-170, Ottawa, June 1987.

26. Mokry, M.; and Ohman, L. H.: Application of the Fast Fourier Transform to Two-Dimensional Wind Tunnel Wall Interference. J. Aircraft, Vol. 17, N. 6, June 1980, pp 402-408.

27. Mokry, M.; and Chan, Y. Y.: Wall Interference Correction from Boundary Measurements. AGARD AG N. 281 on Two-Dimensional Wind Tunnel Interference. Nov. 1983.

28. Stanewsky, E.; Demurie, F.; et al.: High Reynolds Number Tests of the Cast 10-2/DOA-2 Transonic Airfoil at Ambient and Cryogenic Temperature Conditions. AGARD Conference Proceedings on Wind Tunnels and Testing Techniques. N. 348, Paper N. 10, Cesme, Sept. 1983.

29. Arcara, P. C.: CAST 10-2/DOA-2 Airfoil Models Tested in 0.3-m Transonic Cryogenic Tunnel. NASA Unpublished Report.

30. Mineck, R. E.: Wall Interference Tests of a CAST 10-2/DOA-2 Airfoil in an Adaptive Wall Test Section ; NASA TM 4015, Dec. 1987.

31. Murthy, A. V.: Private Communication.

32. Jenkins, R. V.: Private Communication.

33. Mignosi, A.; Saraudie, A.; et al.: Premier Rapport d'Essais du Profil CAST 10 (Chorde = 180 mm) en Transition Naturelle, Effectues dans la Souffleire Transonique Cryogenique T-2 en Presence de Parois Auto-Adaptables ; ONERA/CERT R.T. OA N. 59/1685, Mars 1985.

34. Seraudie, A.; Blanchard, A.; et al.: Rapport d'Essais du Profil CAST 10 en Transition Declenchee, Effectues dans la Souffleire Transonique Cryogenique T-2 en Presence de Parois Auto-Adaptables ; ONERA/CERT, R.T. OA N. 63/1685, Aout 1985.

35. Green, L. L.; and Newman, P. A.: Transonic Wall Interference and Correction for Airfoil Data from the 0.3-m TCT Adaptive Wall Test Section ; AIAA 19th Fluid-dynamics, Plasma Dynamics Conference, Honolulu, June 1987.

36. Melnik, R. E.; Chow, R. R.; et al.: An Improved Viscid/Inviscid Interaction Procedure for Transonic Flow over Airfoils ; NASA CR 3805, Oct. 1985.

37. Mead, H. R.; and Melnick, R. E.: GRUMFOIL: A Computer Code for the Viscous Transonic Flow over Airfoil ; NASA CR 3806, Oct. 1985.

38. McCroskey, W. J.: A Critical Assessment of the Wind Tunnel Results for the NACA 0012 Airfoil ; AGARD FDP Symposium on Aerodynamic Data Accuracy and Quality: Requirement and Capabilities in Wind Tunnel Testing , Paper N.1, Naples, Sept. 1987.

39. Johnson, W. G.; Hill, A. S.; at al.: High Reynolds Number Tests of a BOEING BAC I Airfoil in the Langley 0.3-Meter Transonic Cryogenic Tunnel ; NASA TM 81922, Apr. 1982.

9.   ACKNOWLEDGMENT

Hampton, Va.
August 7, 1989

```
                    ┌─────────┐
                    │  START  │
                    └────┬────┘
                         │
          ┌──────────────▼──────────────┐
          │  SET UP TUNNEL AND MODEL    │
          │  CONDITIONS                 │
          └──────────────┬──────────────┘
                         │
          ┌──────────────▼──────────────┐
          │  INITIALIZE THE SHAPE OF    │
          │  THE CONTROL BOUNDARY "S"   │
          └──────────────┬──────────────┘
                         │
          ┌──────────────▼──────────────┐
          │  MEASURE TWO INDEPENDENT    │
          │  FLOW VARIABLES pr, qr ON "S"│
          └──────────────┬──────────────┘
                         │
          ┌──────────────▼──────────────┐
          │  CALCULATE pf USING THE     │
          │  BOUNDARY CONDITION qr ON "S"│
          └──────────────┬──────────────┘
                         │
                    ╱────▼────╲
                   ╱  |pf-pr|  ╲   yes
                  ╱    < ε  ?    ╲────────►  TAKE MODEL DATA
                   ╲           ╱                   │
                    ╲─────────╱                    ▼
                     no  │                        STOP
          ┌─────────────▼───────────────┐
          │  CALCULATE THE SHAPE OF THE │
          │  BOUNDARY "S" FOR STEAMLINING│
          └─────────────┬───────────────┘
                        ▼
                  ┌───────────┐
                  │ ADJUST "S"│
                  └───────────┘
```
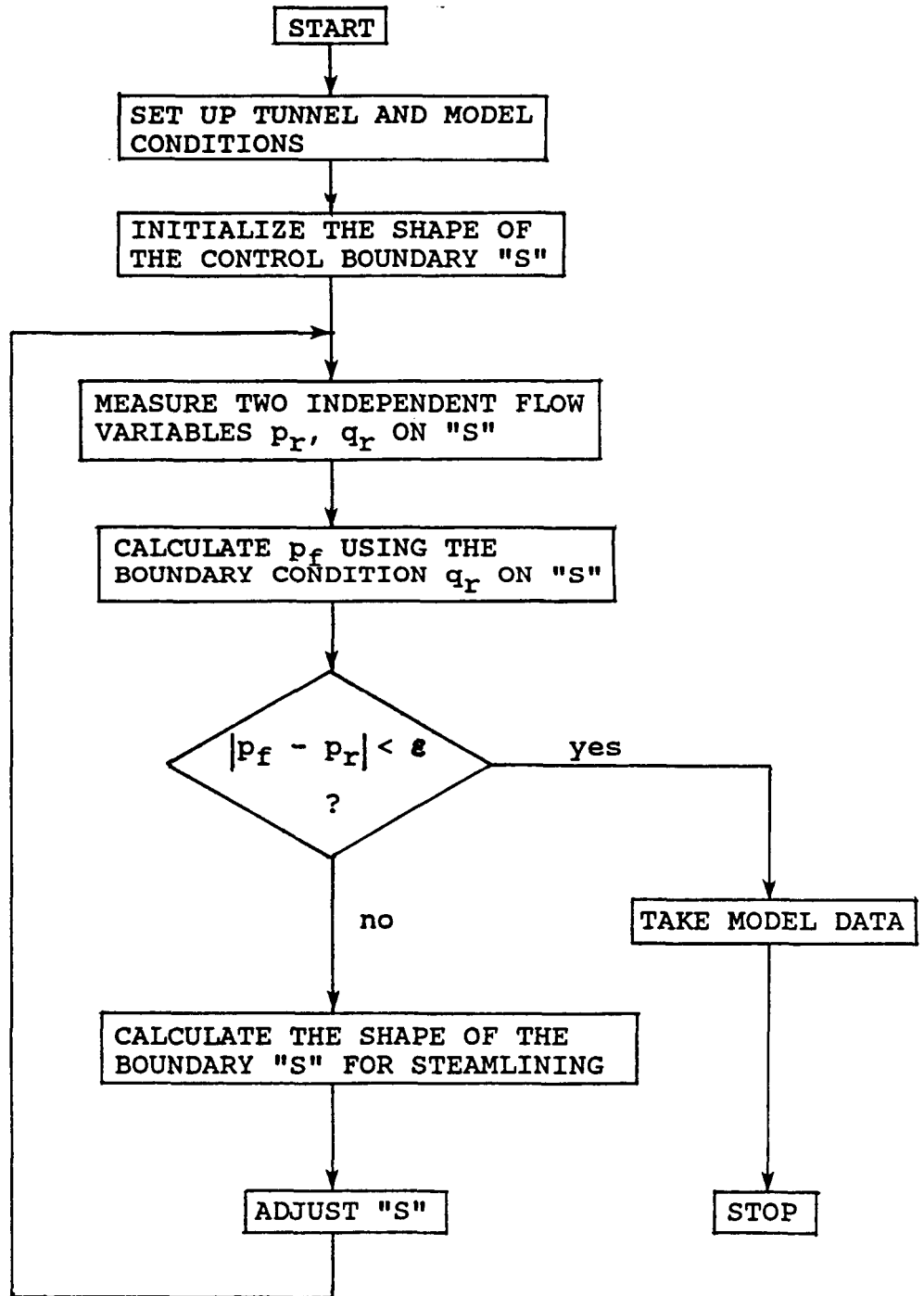
Figure 1. - Flow chart of wall adaptation principle.
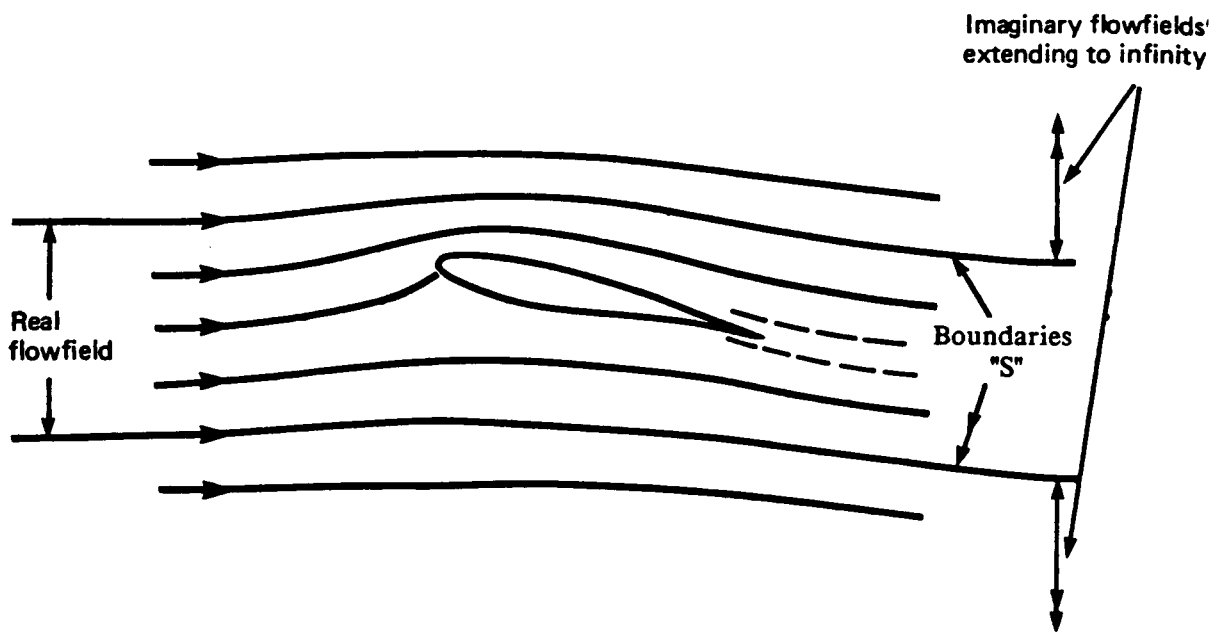
Figure 2. - Artistic illustration of 2-D wall adaptation principle (from Ref. 5).

NASA 0.3-m TCT
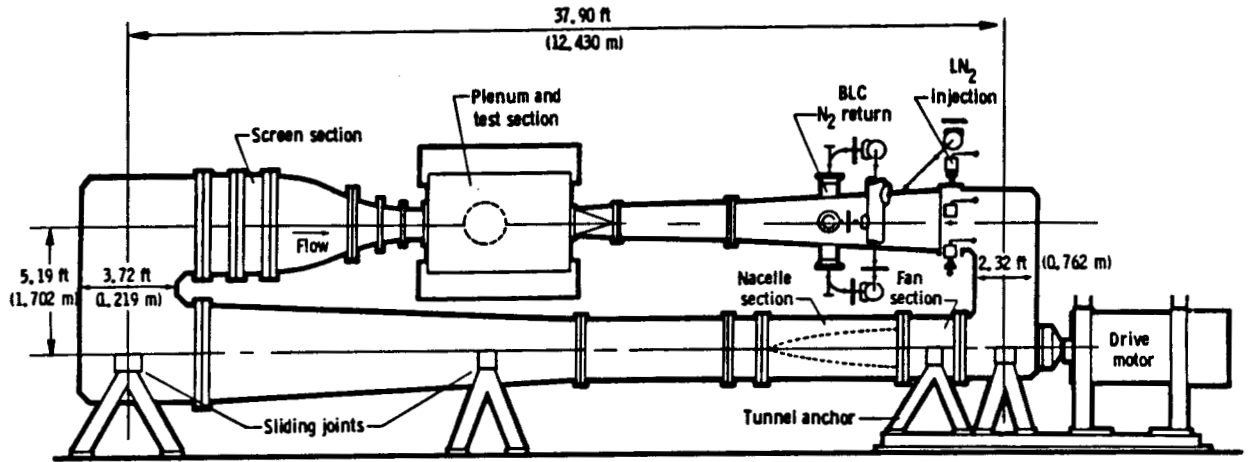
ONERA T-2
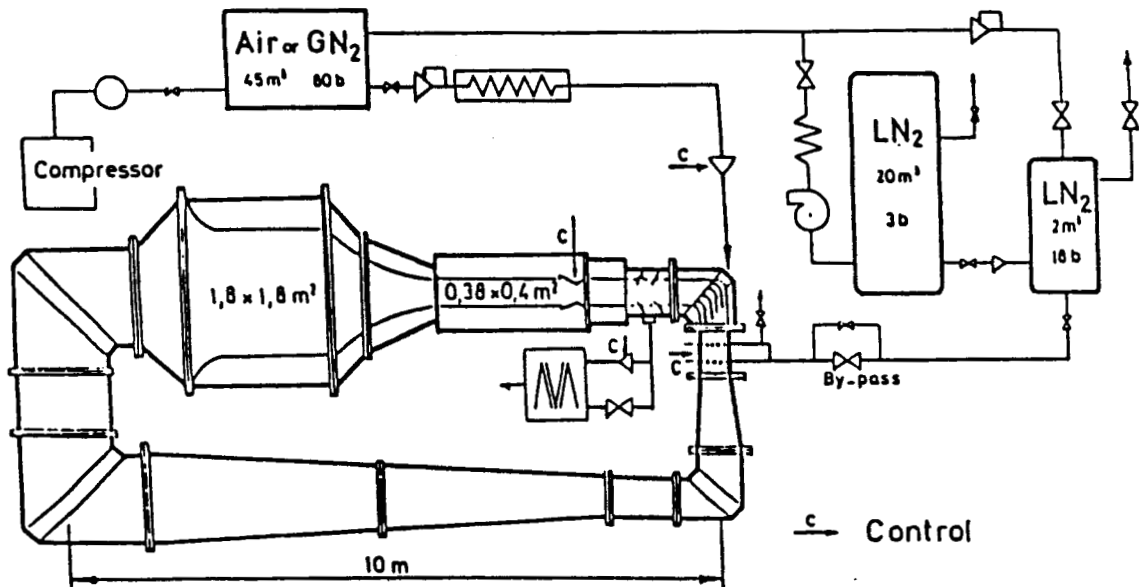
Figure 3. - Schematics of NASA 0.3-m TCT and ONERA T-2.
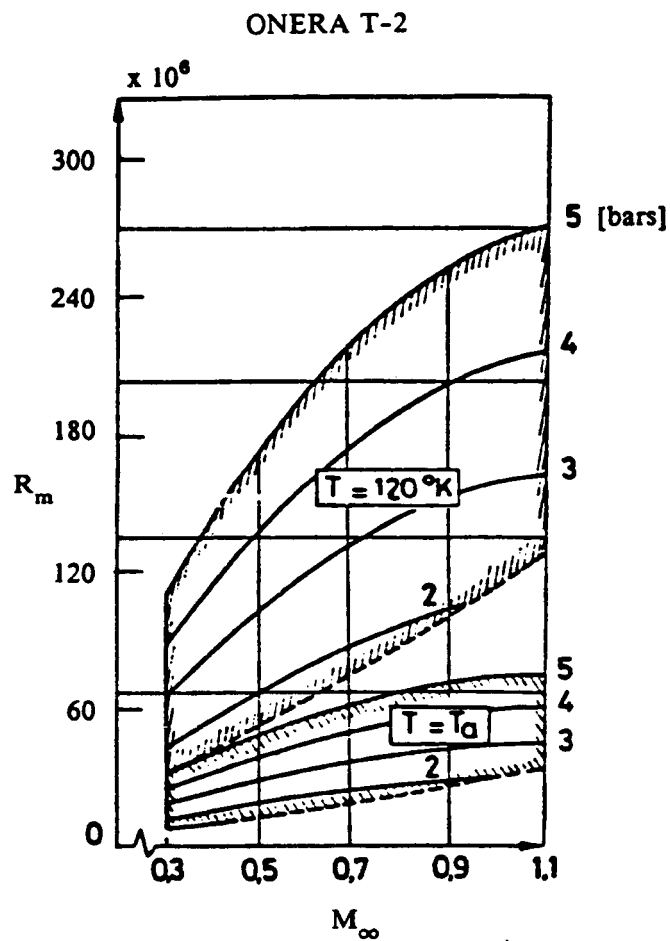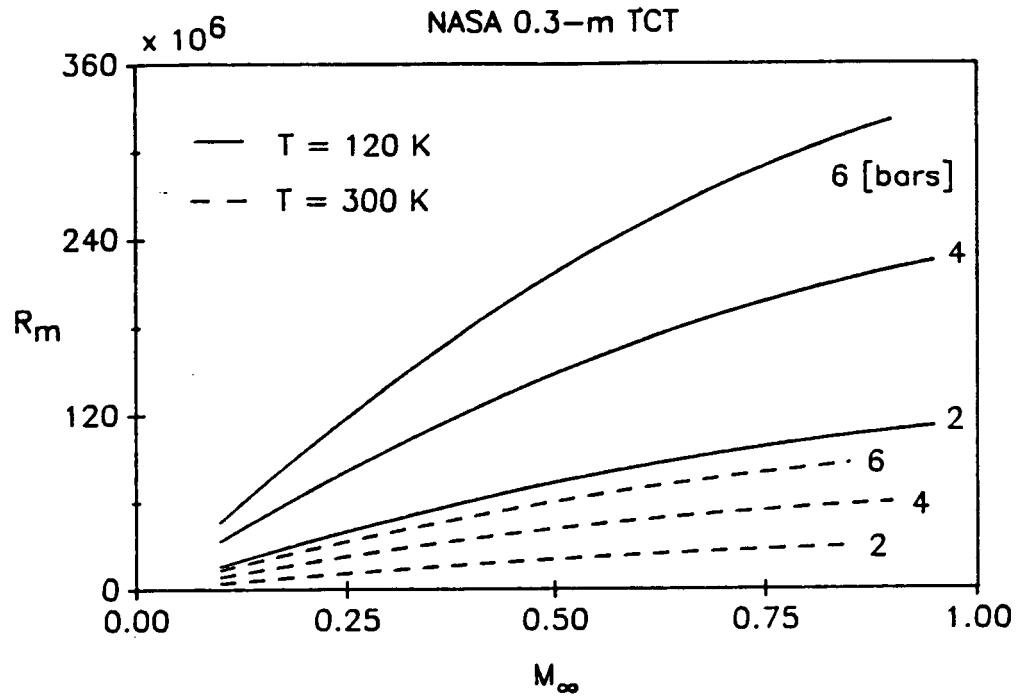
Figure 4. - Operating envelopes of NASA 0.3-m TCT and ONERA T-2 (from Ref. 11) at several stagnation pressures and temperatures.

NASA 0.3-m TCT
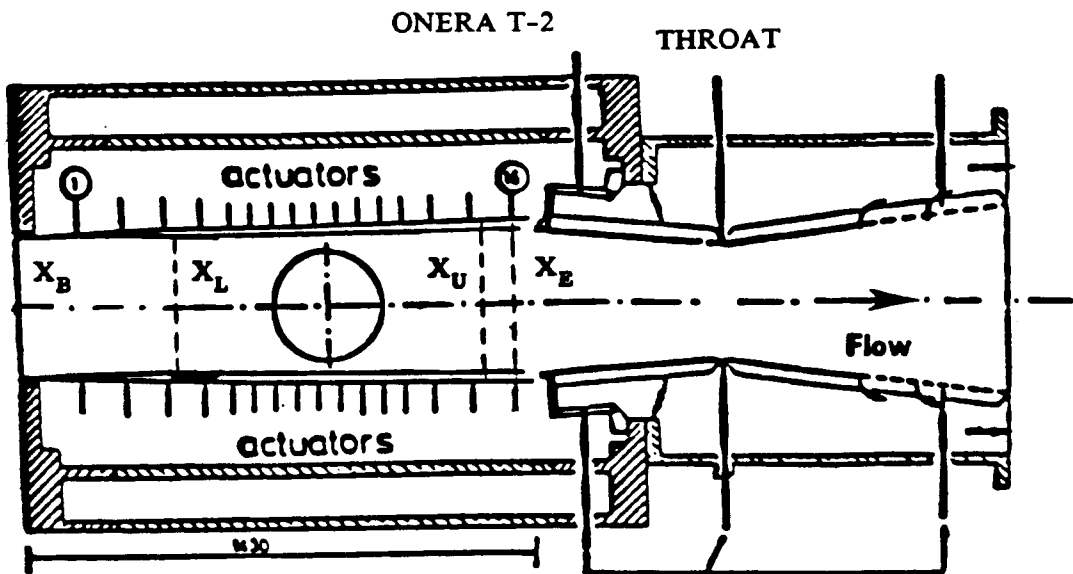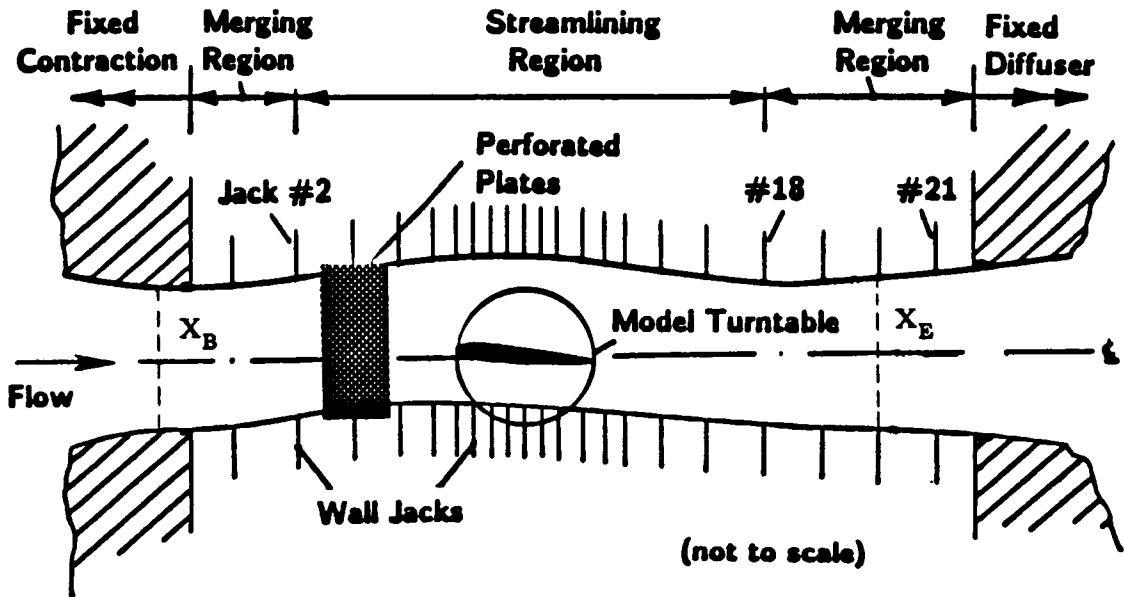
ONERA T-2

Figure 5. - Schematics of test sections of NASA 0.3-m TCT and ONERA T-2.
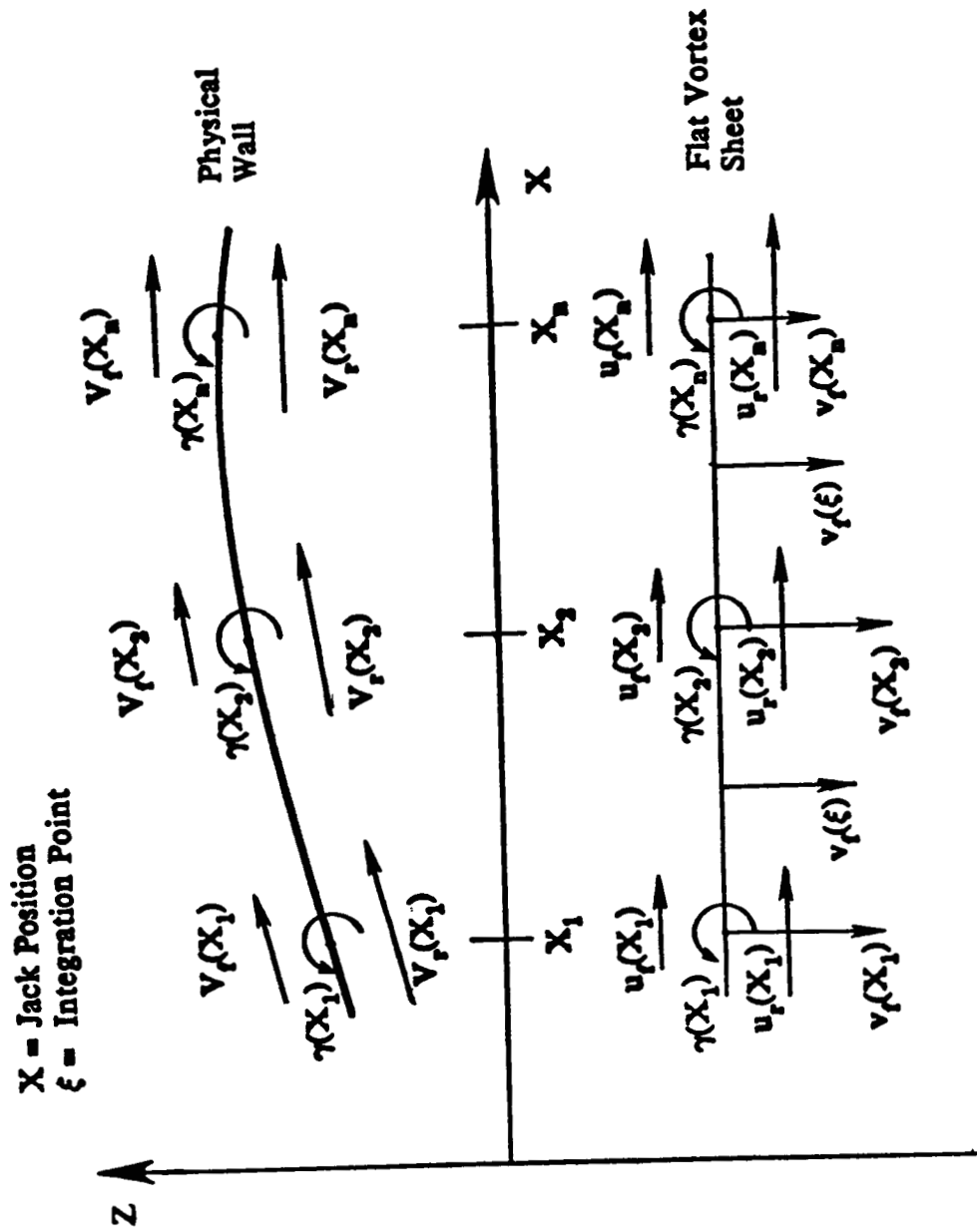
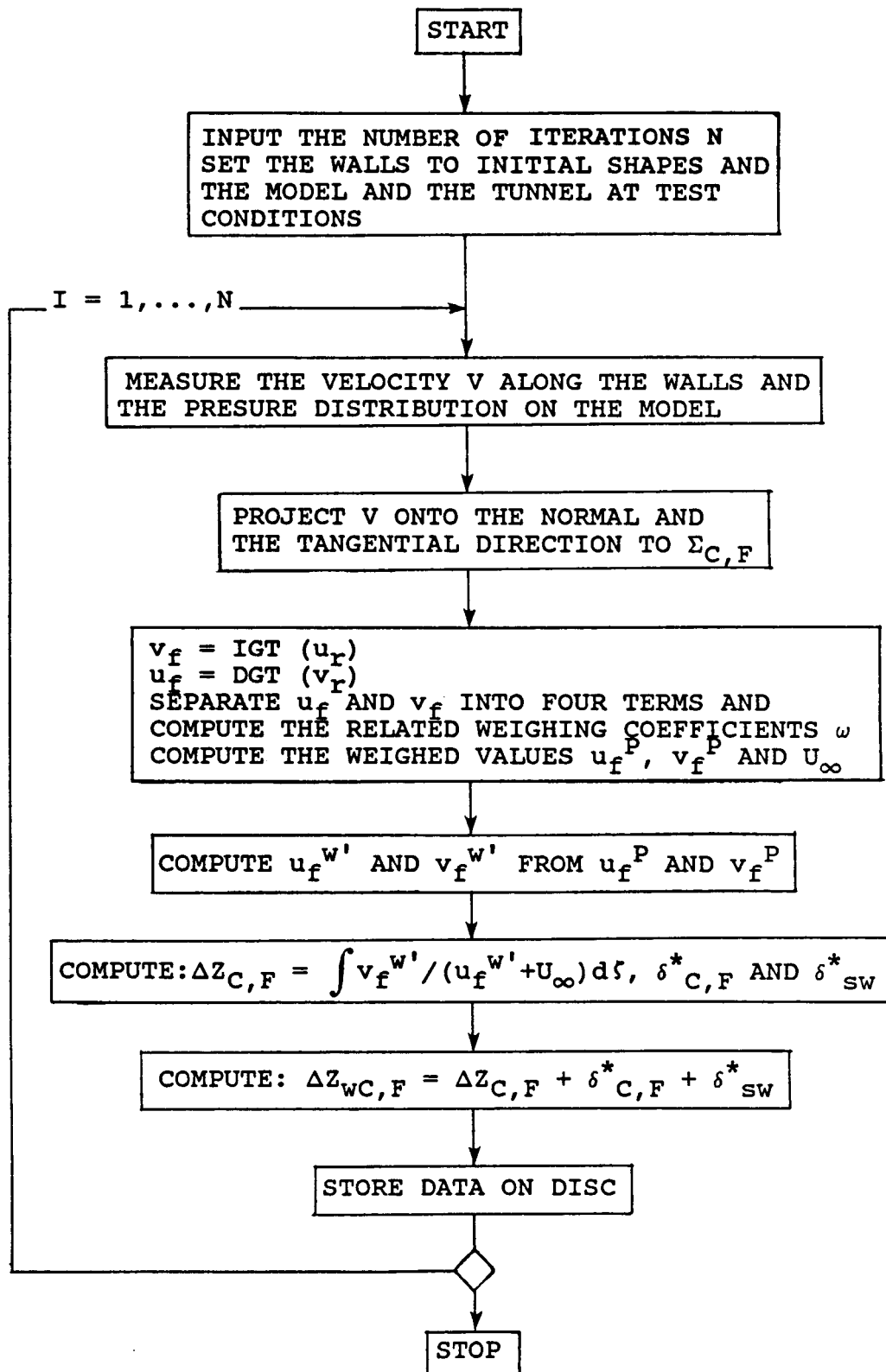Figure 6. - Representation of physical wall as a flat vortex sheet by NASA wall adaptation strategy.

33

```
                        ┌─────────┐
                        │  START  │
                        └─────────┘
                             │
                             ▼
        ┌──────────────────────────────────────────┐
        │ INPUT THE NUMBER OF ITERATIONS N          │
        │ SET THE WALLS TO INITIAL SHAPES AND       │
        │ THE MODEL AND THE TUNNEL AT TEST          │
        │ CONDITIONS                                │
        └──────────────────────────────────────────┘
                             │
   ┌─ I = 1,...,N ───────────┤
   │                         ▼
   │    ┌──────────────────────────────────────────┐
   │    │ MEASURE THE VELOCITY V ALONG THE WALLS AND│
   │    │ THE PRESURE DISTRIBUTION ON THE MODEL     │
   │    └──────────────────────────────────────────┘
   │                         │
   │                         ▼
   │       ┌───────────────────────────────────────┐
   │       │ PROJECT V ONTO THE NORMAL AND          │
   │       │ THE TANGENTIAL DIRECTION TO Σ_{C,F}    │
   │       └───────────────────────────────────────┘
```
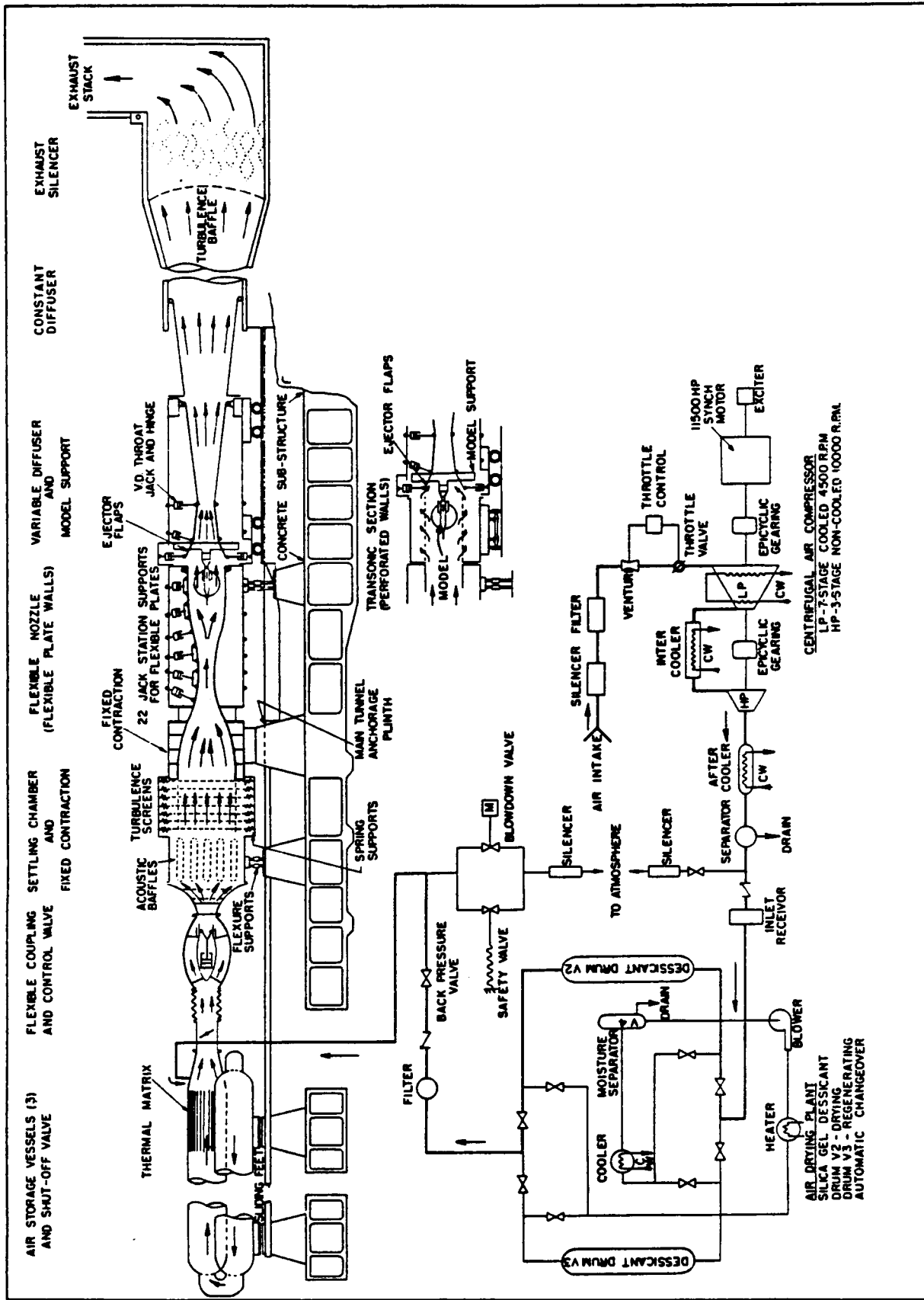
Figure 8. – Schematic of NAE 5'x5' tunnel.
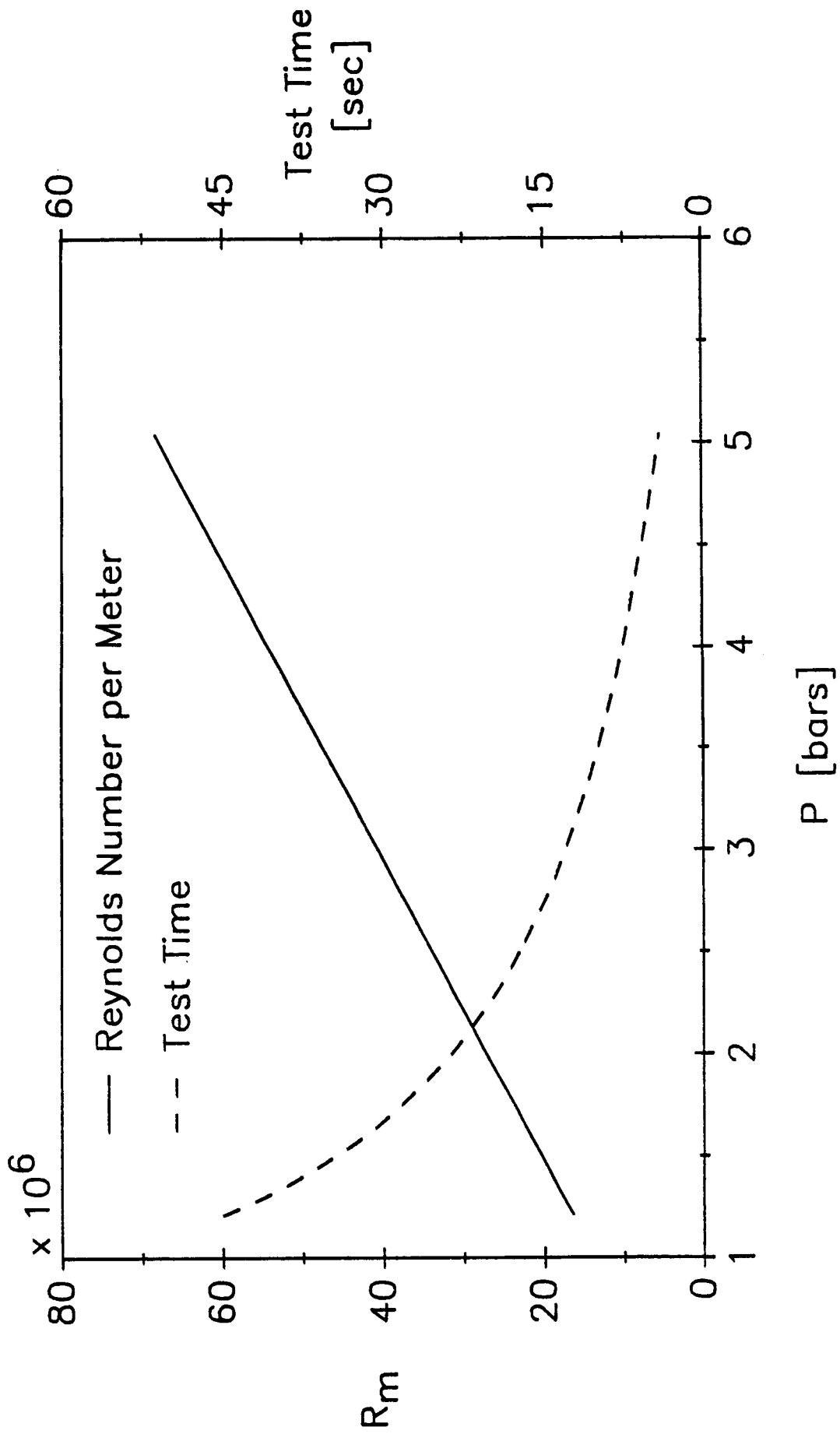
Figure 9. - Estimated test time and Reynolds number per meter of NAE 5'x5' tunnel as a function of the stagnation pressure at $M_\infty = 0.75$
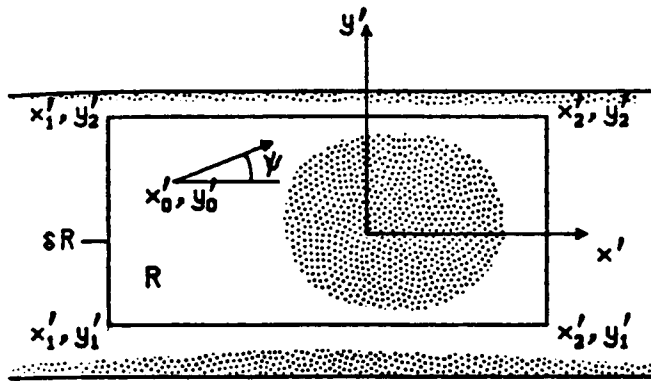
Figure 10. - Coordinate system of Mokry's method (from Ref. 26).
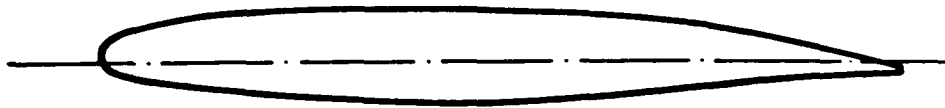
```
Geometrical characteristics:
Max. percentage thickness = 0.121 at x/c = 0.45
Trailing edge percentage thickness = 0.005

Aerodynamic design characteristics:
```
$M_\infty = 0.76$, $C_l = 0.595$, $\alpha = 0.3$ deg.

Figure 11. - Sketch of CAST 10-2/DOA-2 airfoil.
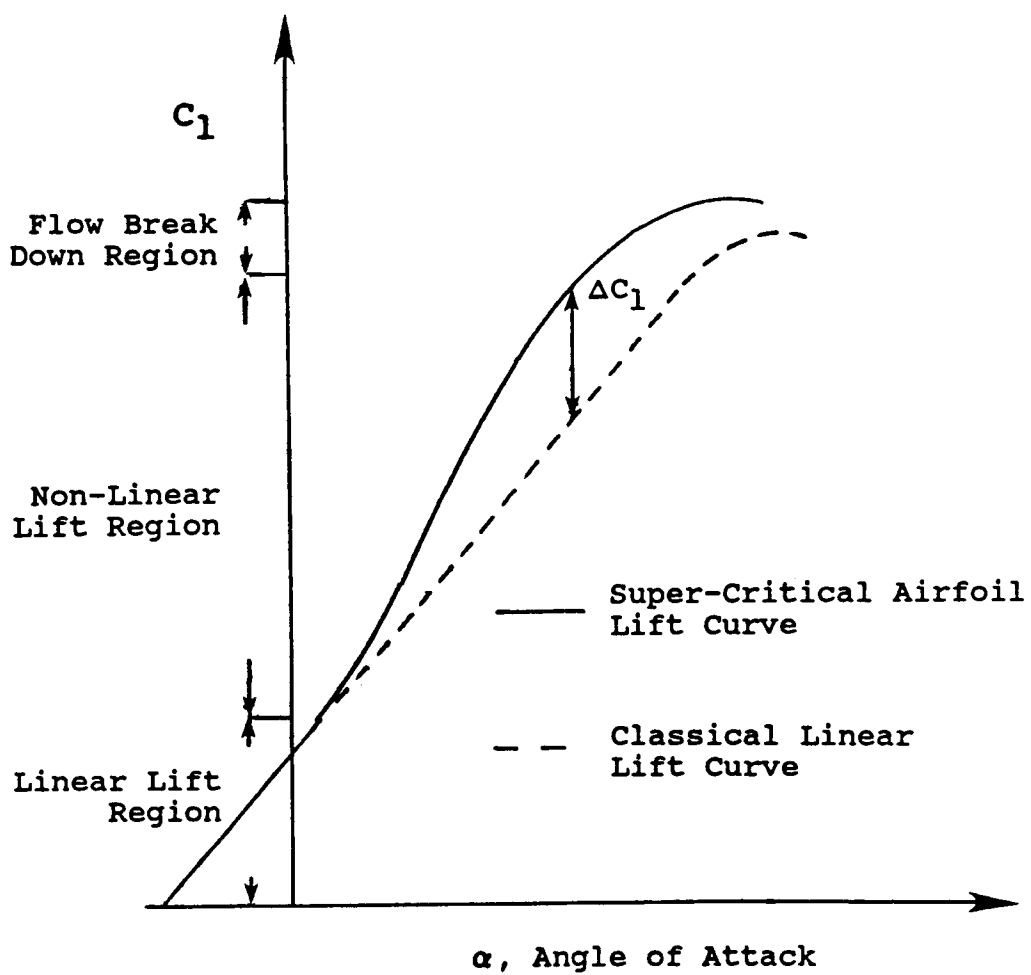
Figure 12. - Artistic illustration of the lift curve of a super-critical airfoil.
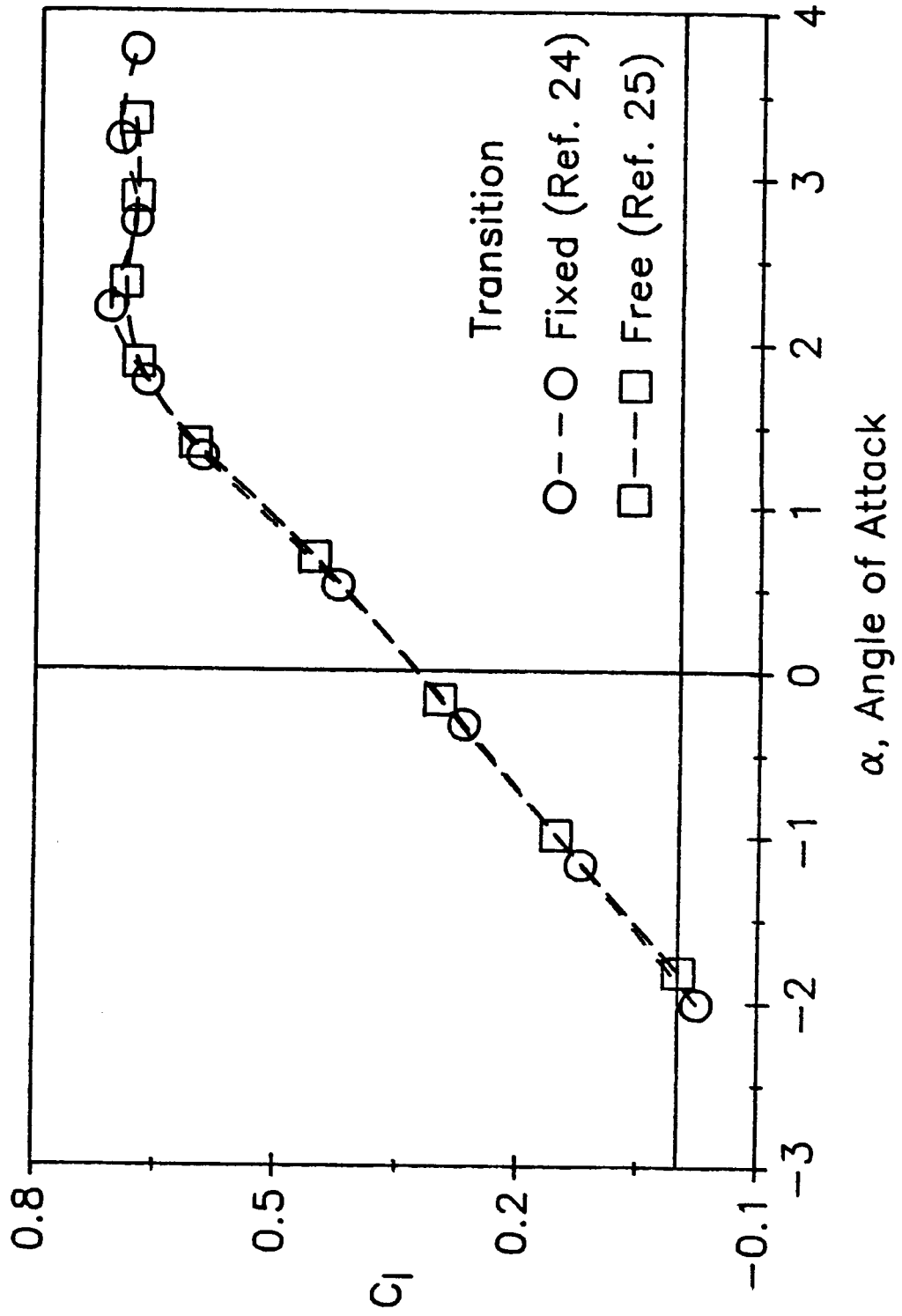
Figure 13. - Lift curves of the Canadian CAST 10 airfoil model from the NAE 5'x5' tunnel, $M_\infty \approx 0.765$, $R_c \approx 20 \times 10^6$.

40
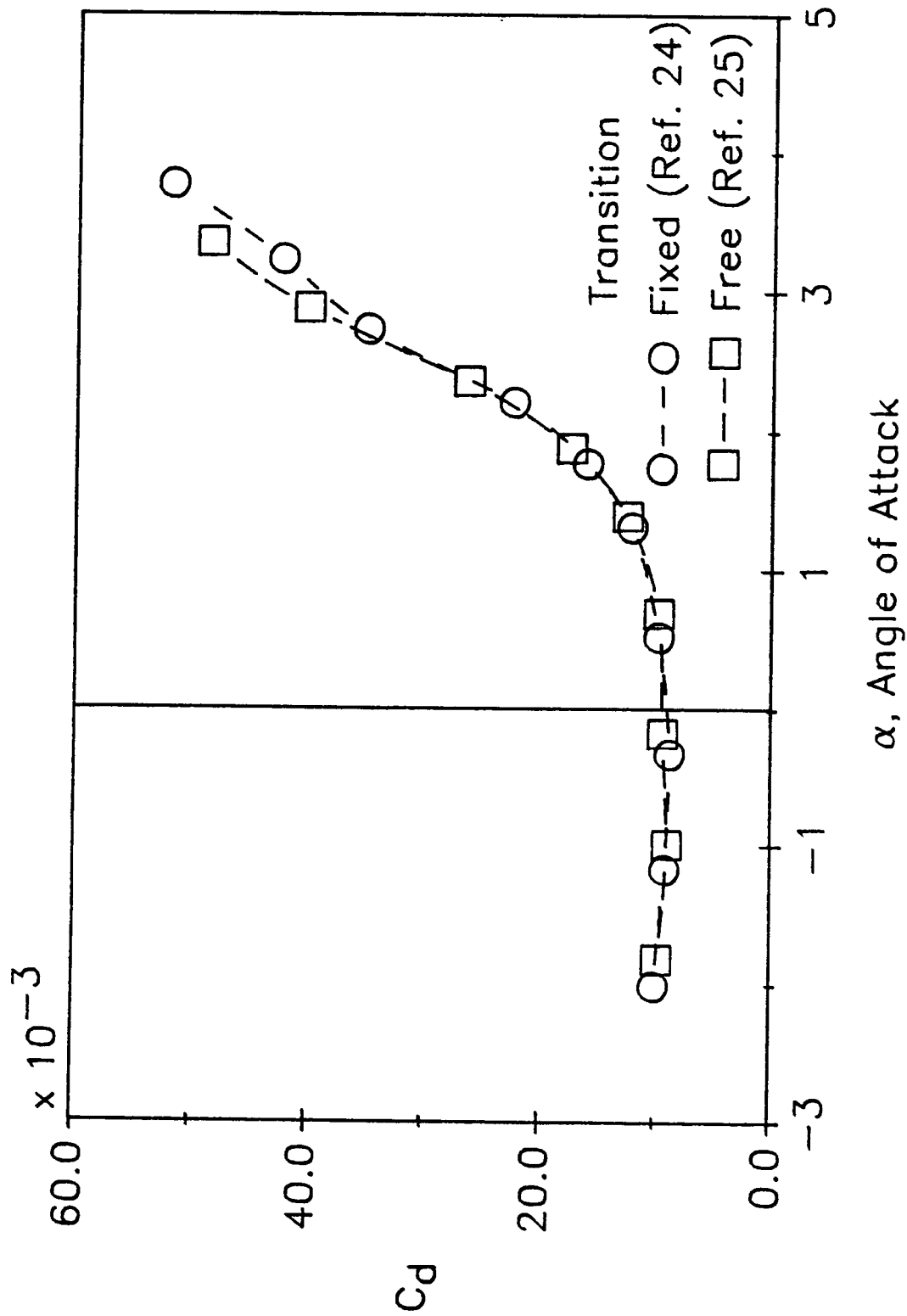
Figure 14. – Drag curves of the Canadian CAST 10 airfoil model with free and fixed
transition from the NAE 5'x5' tunnel, $M_\infty \approx 0.765$, $R_c \approx 20 \times 10^6$.
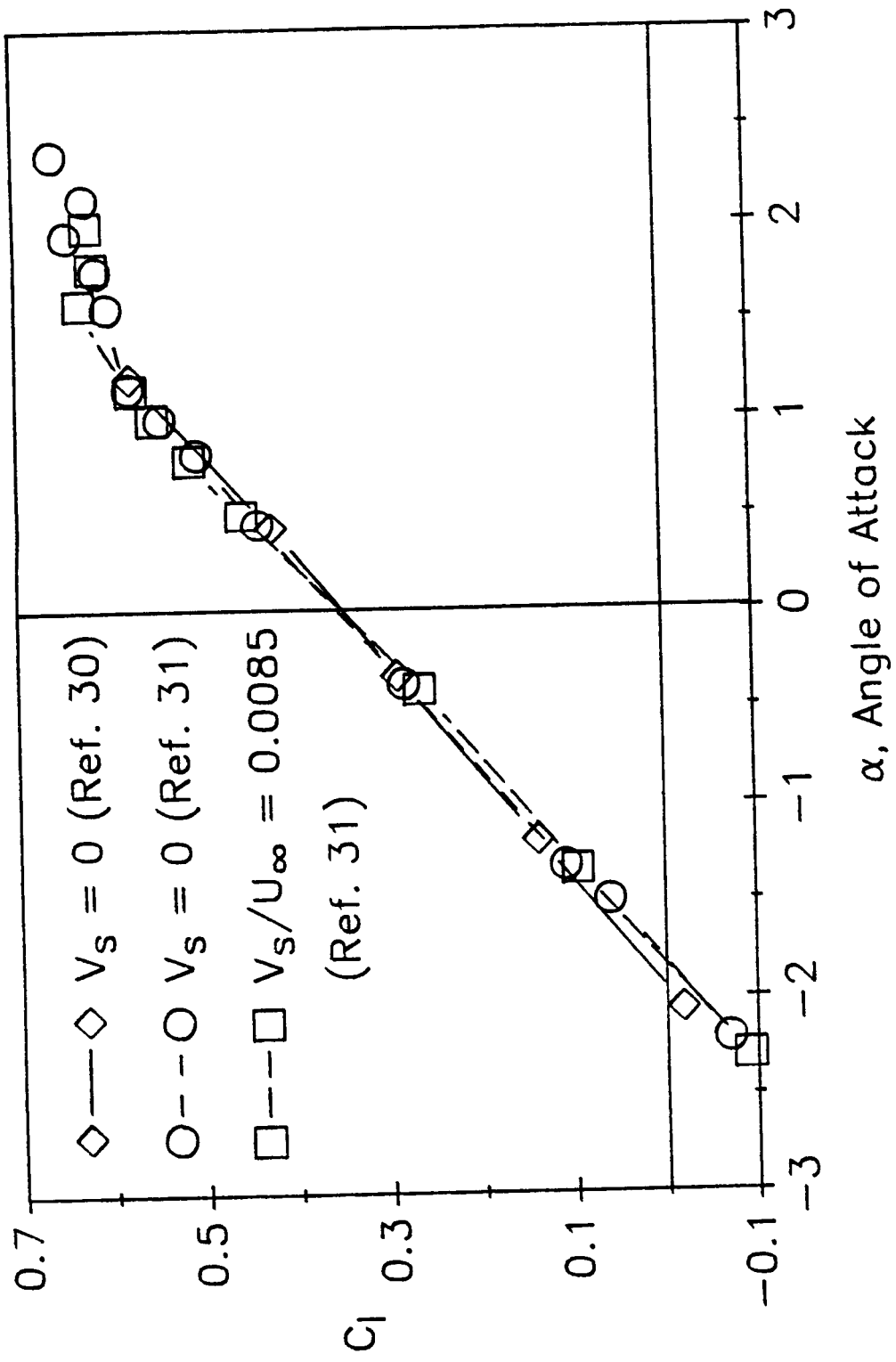
Figure 15. - Lift curves of the Canadian CAST 10 airfoil model from the NASA 0.3-m TCT, $M_\infty \approx 0.765$, $R_c \approx 20 \times 10^6$, Fixed Transition.
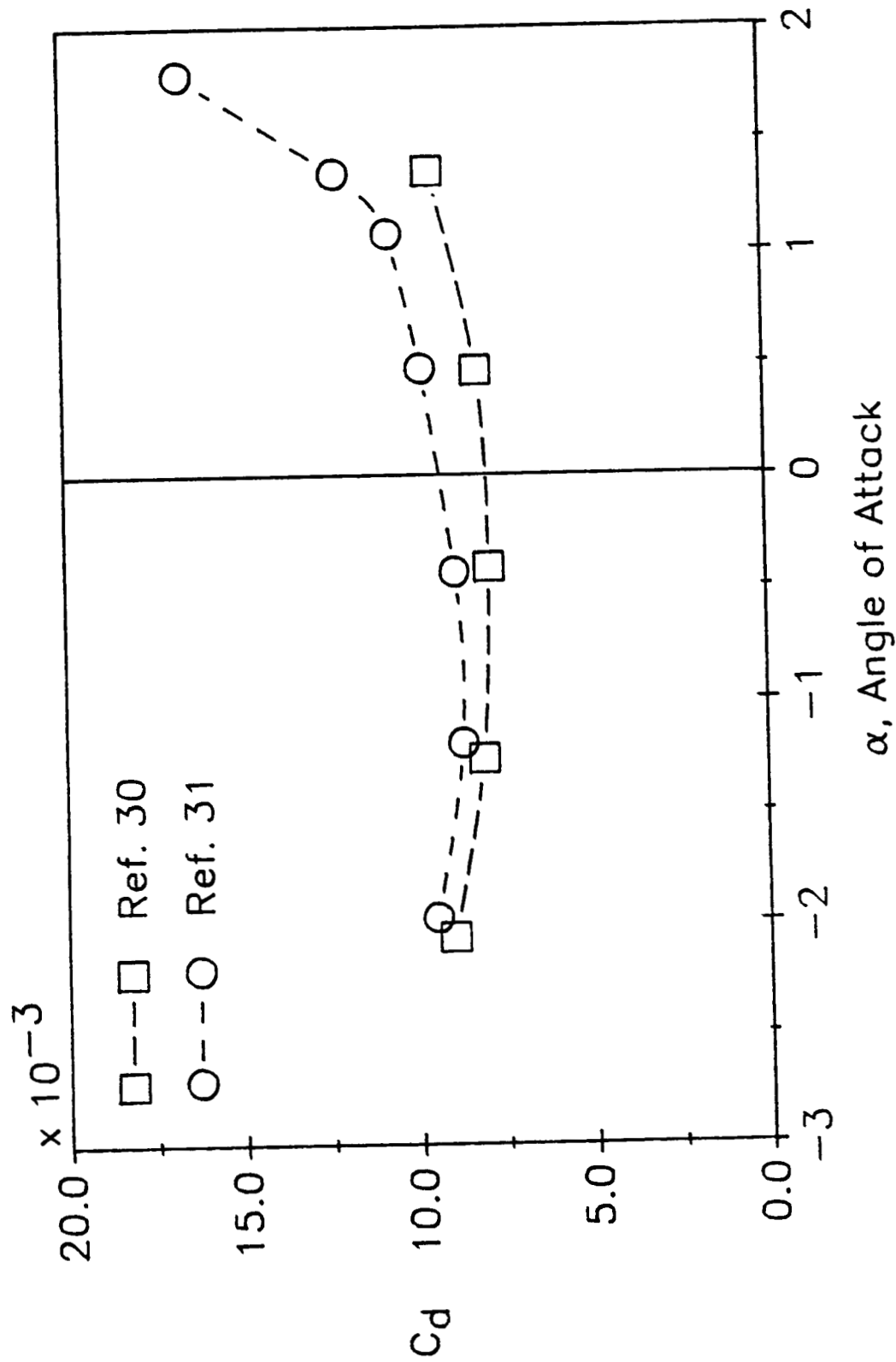
Figure 16. - Drag curves of the Canadian CAST 10 airfoil model from the NASA 0.3-m TCT, $M_\infty \approx 0.750$, $R_c \approx 20 \times 10^6$, Fixed Transition.
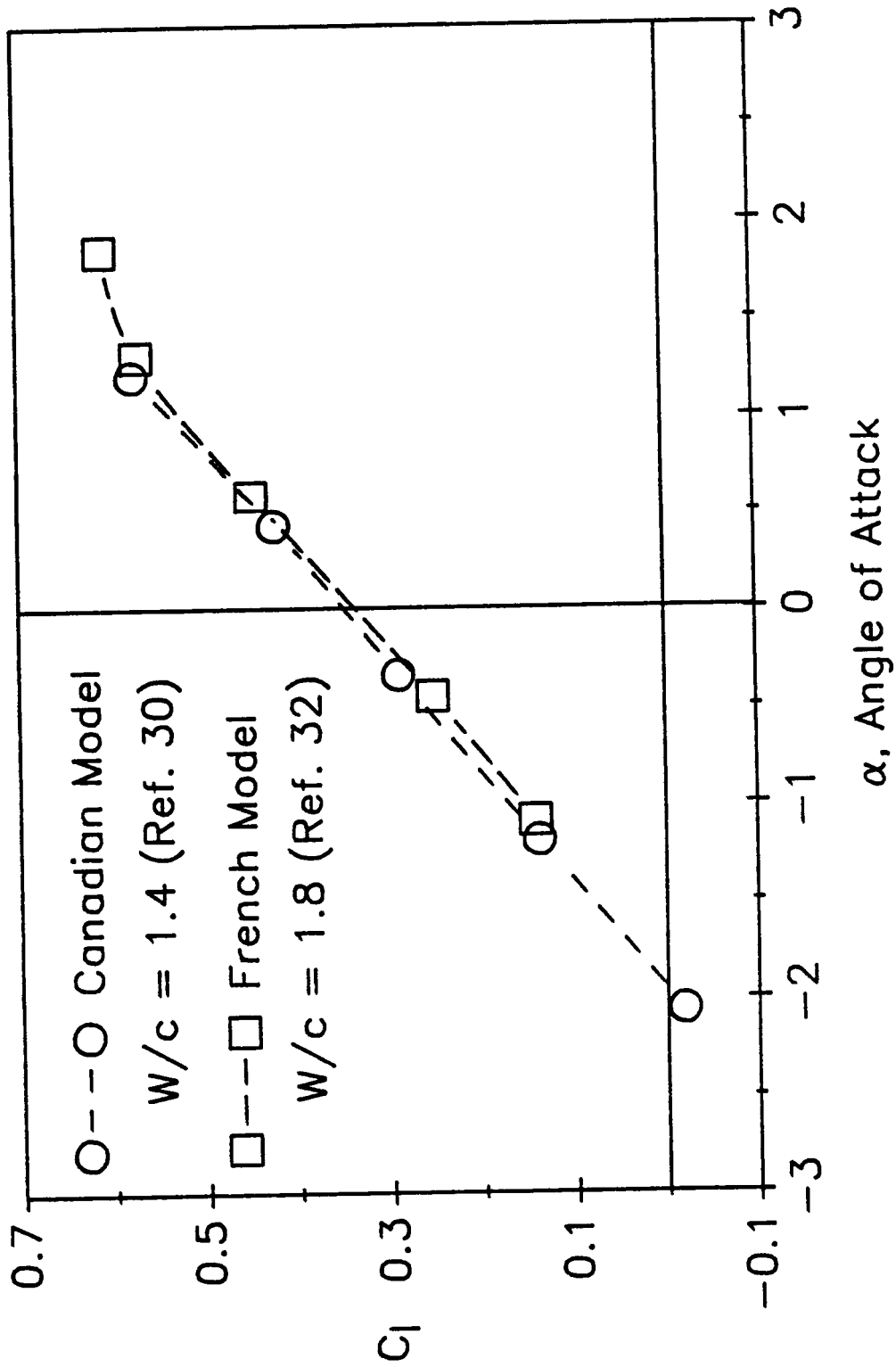
Figure 17.- Lift curves of the Canadian and French CAST 10 airfoil model from the NASA 0.3-m TCT, $M_\infty \approx 0.765$, $R_c \approx 20 \times 10^6$, Fixed Transition.
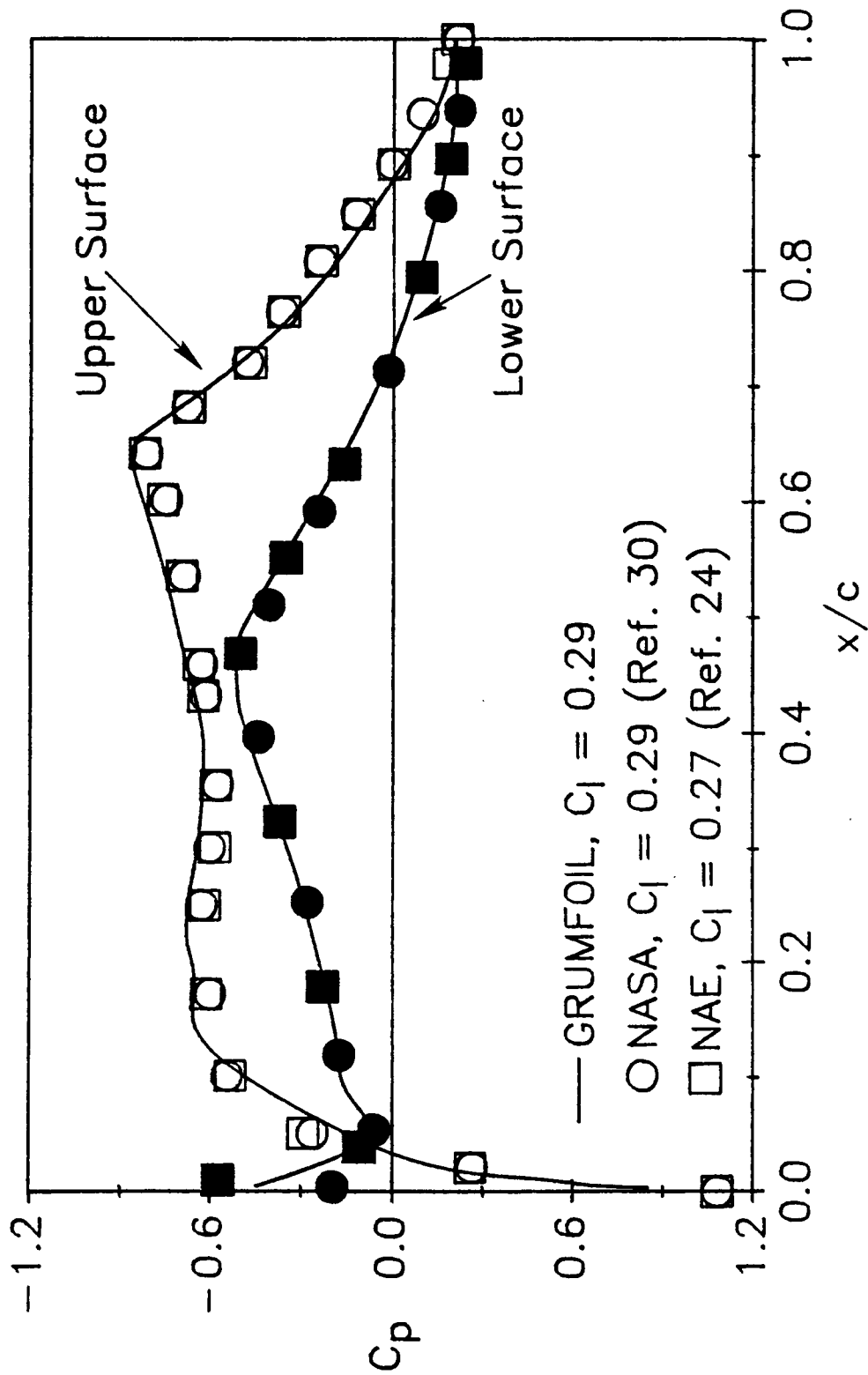
Figure 18. – Pressure distribution on the Canadian CAST 10 airfoil model from the NASA 0.3-m TCT, NAE 5'x5' tunnel, and GRUMFOIL code, $M_\infty \approx 0.765$, $R_c \approx 20 \times 10^6$, Fixed Transition.
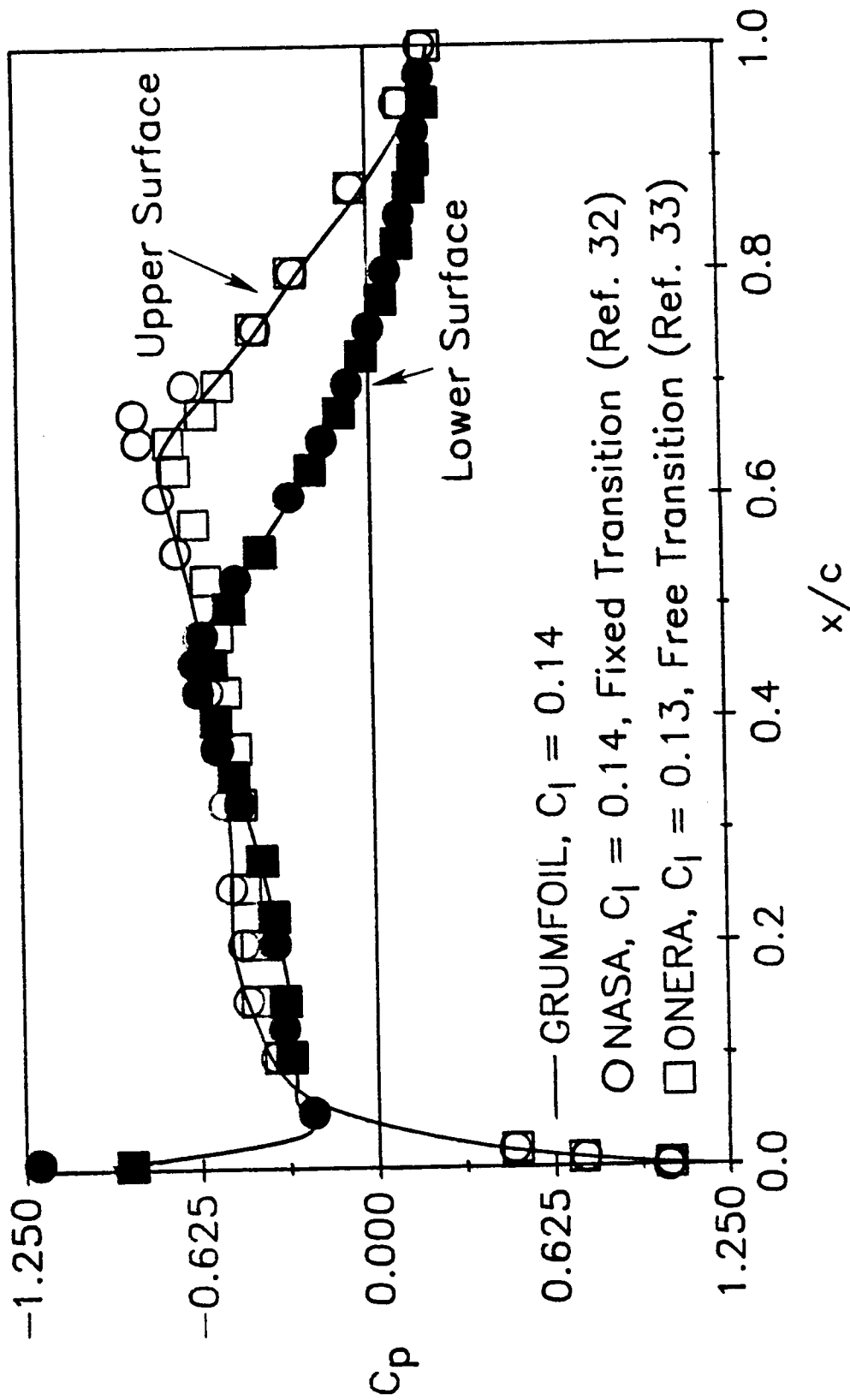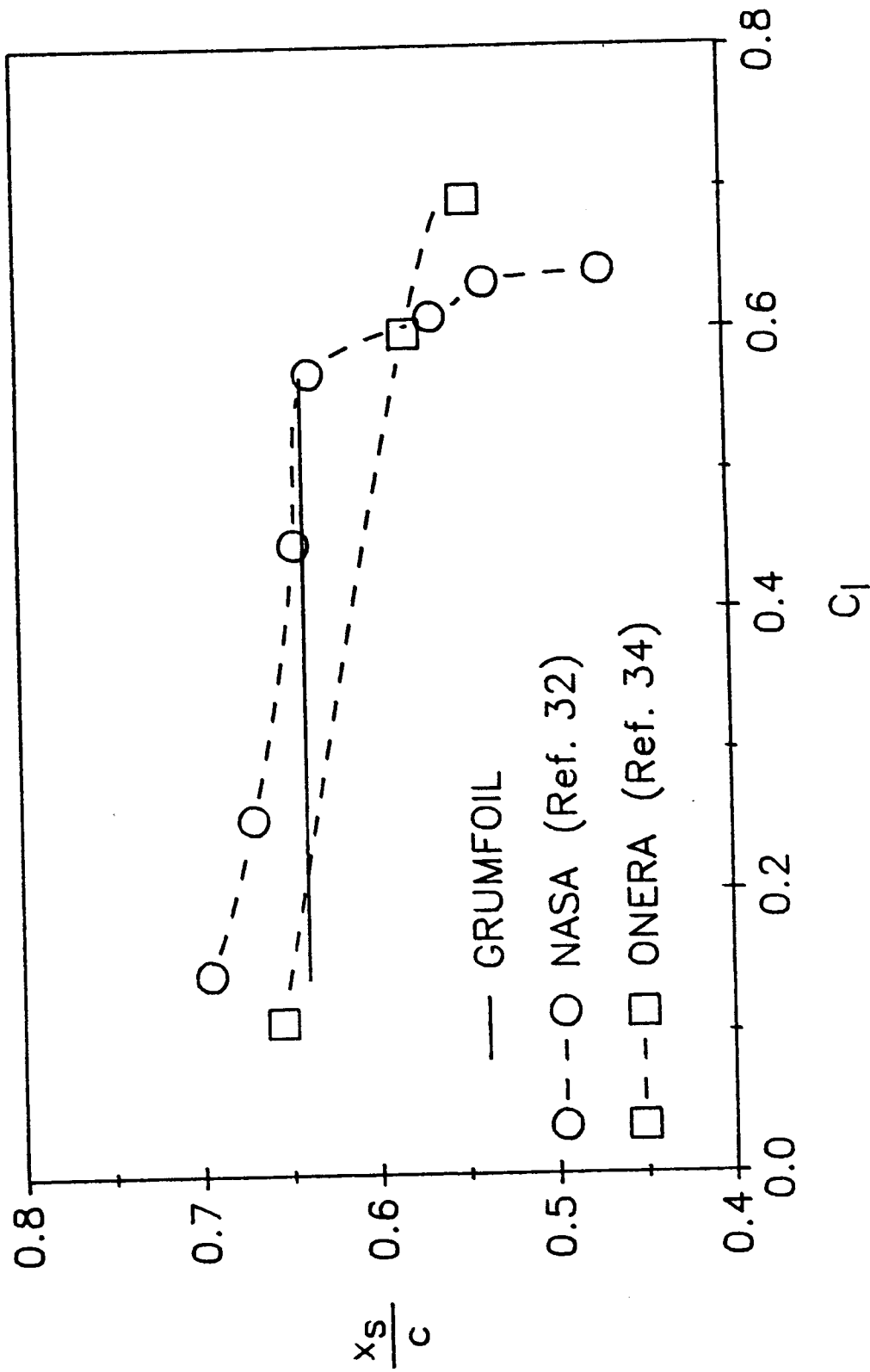
Figure 19. - Pressure distribution on the French CAST 10 airfoil model from the NASA 0.3-m TCT, ONERA T-2 tunnel, and GRUMFOIL code, $M_\infty \approx 0.765$, $R_c \approx 20 \times 10^6$.

46
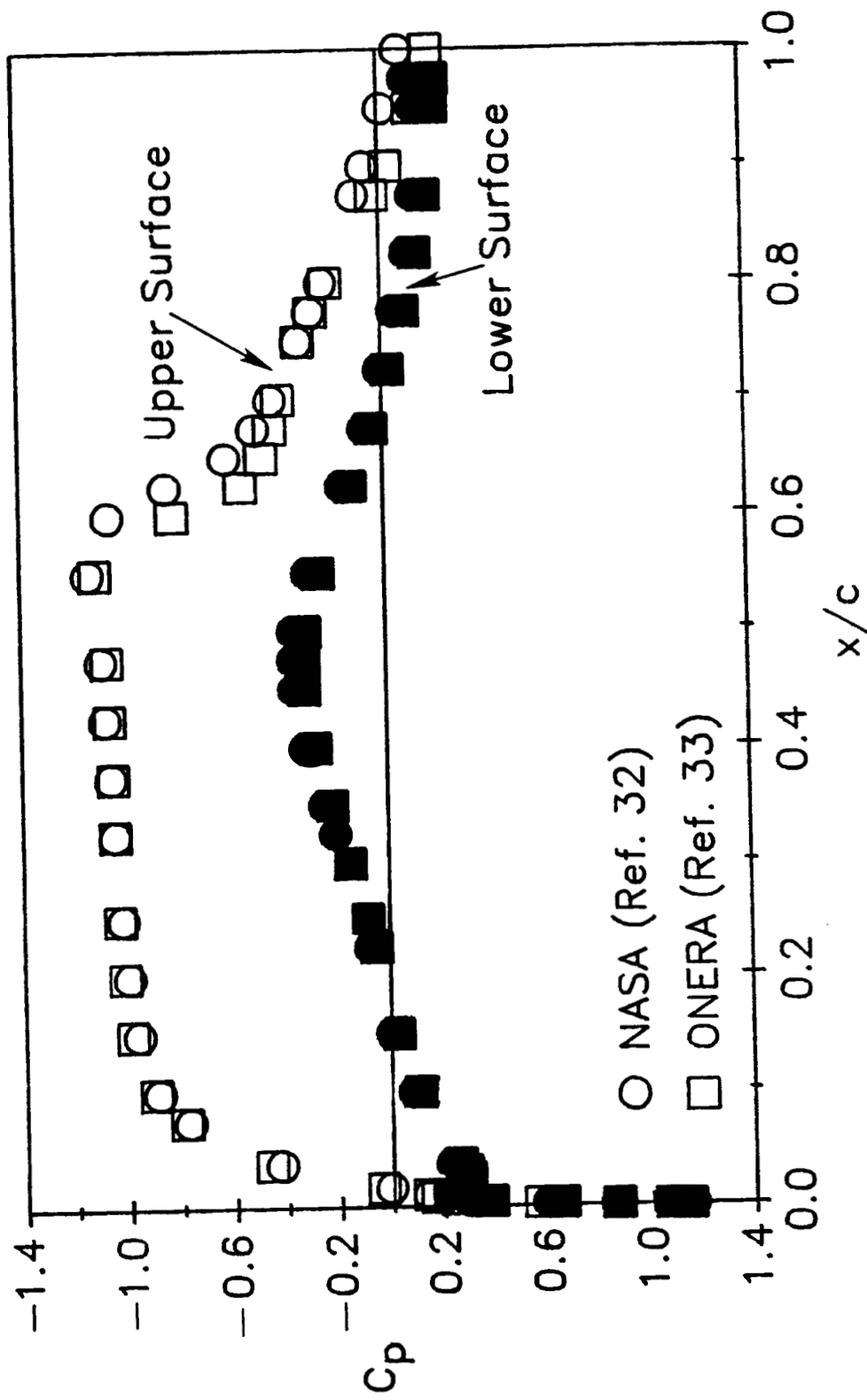
Figure 20. - Pressure distribution on the French CAST 10 airfoil model from the NASA 0.3-m TCT and ONERA T-2 tunnel, $M_\infty \approx 0.765$, $R_c \approx 20 \times 10^6$, $C^1 \approx 0.62$, Free Transition.

47
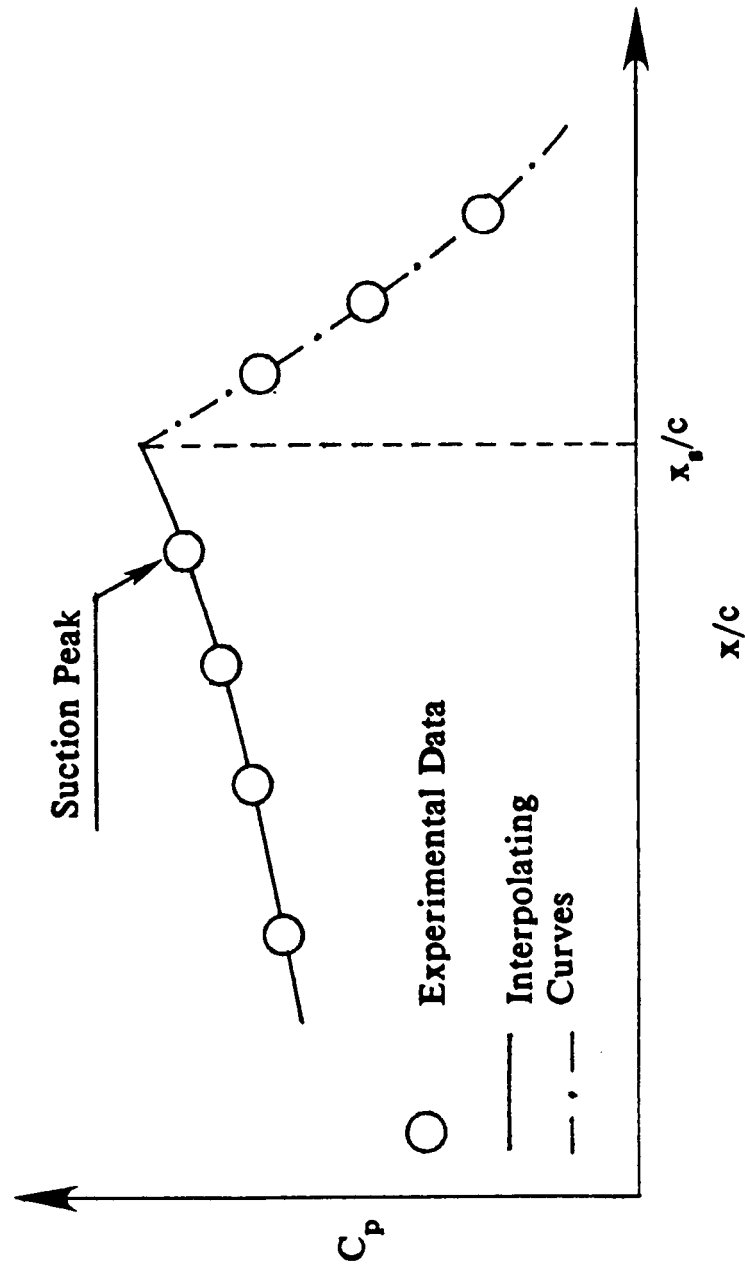
Figure 21. – Artistic illustration of the criterion to locate the shock wave on the airfoil upper surface.
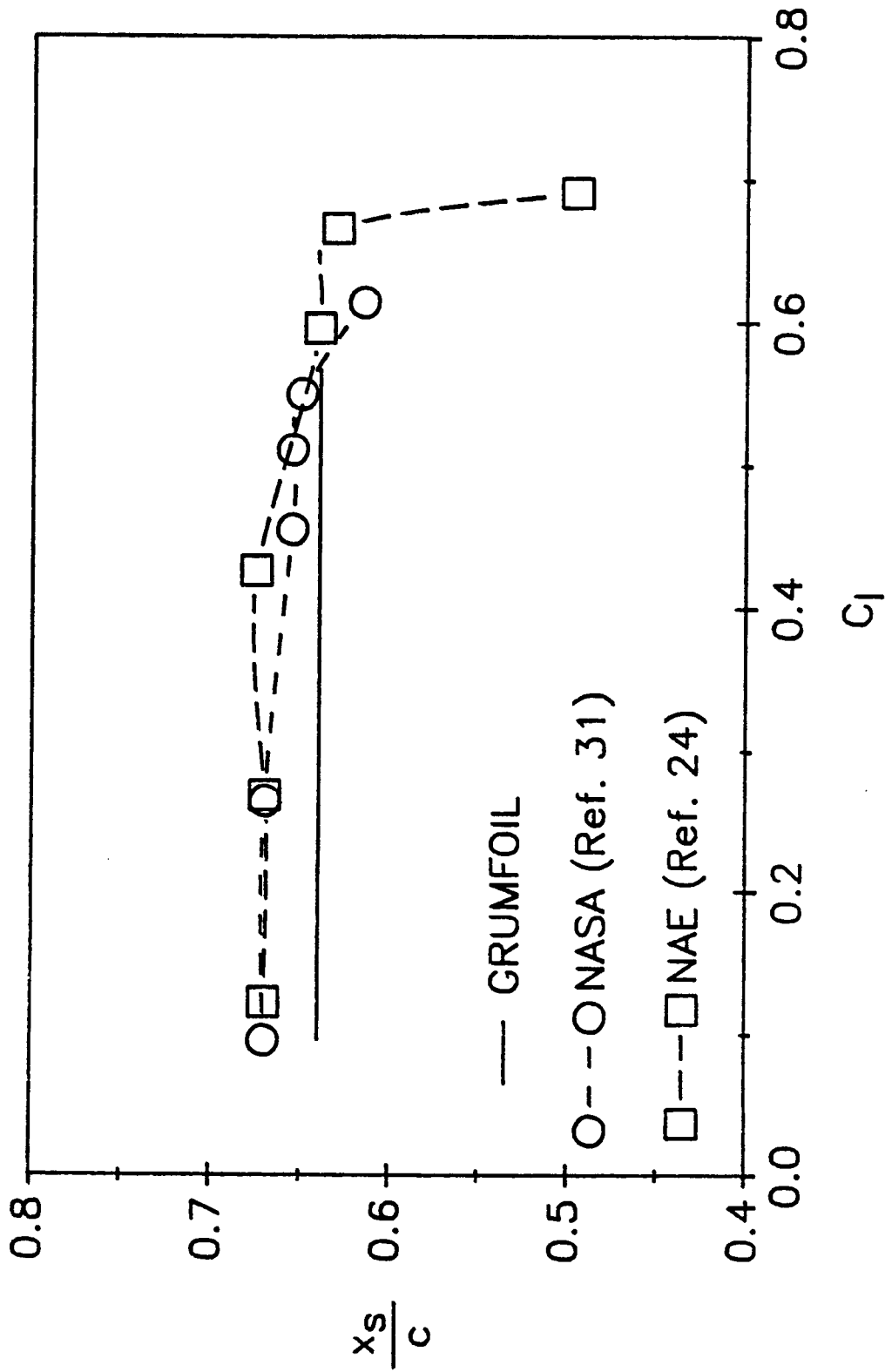
Figure 22. - Shock location on the Canadian CAST 10 airfoil model as a function of the lift coefficient from the NASA 0.3-m TCT, NAE 5'x5' tunnel, and GRUMFOIL code, $M_\infty \approx 0.765$, $R_c \approx 20 \times 10^6$, Fixed Transition.
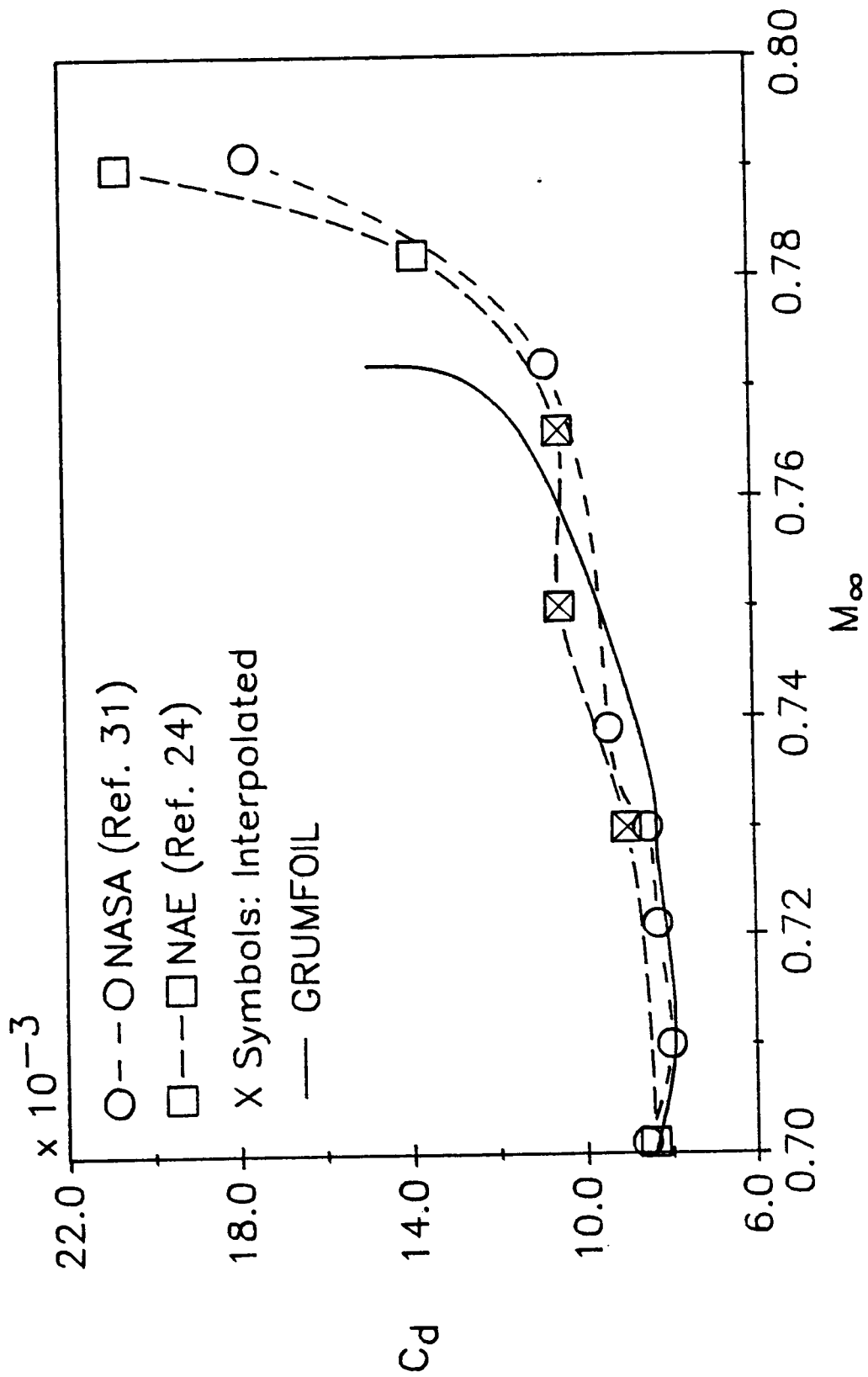
49

Figure 23. – Shock location on the French CAST 10 airfoil model as a function of the lift coefficient from the NASA 0.3-m TCT, ONERA T-2 tunnel, and GRUMFOIL code, $M_\infty \approx 0.765$, $R_c \approx 20 \times 10^6$, Fixed Transition.

Figure 24. - Drag curves of the Canadian CAST 10 airfoil model as a function of the Mach number from the NASA 0.3-m TCT, NAE 5'x5' tunnel, and GRUMFOIL code, $R_c \approx 20 \times 10^6$, $C^1 \approx 0.5$, Fixed Transition.
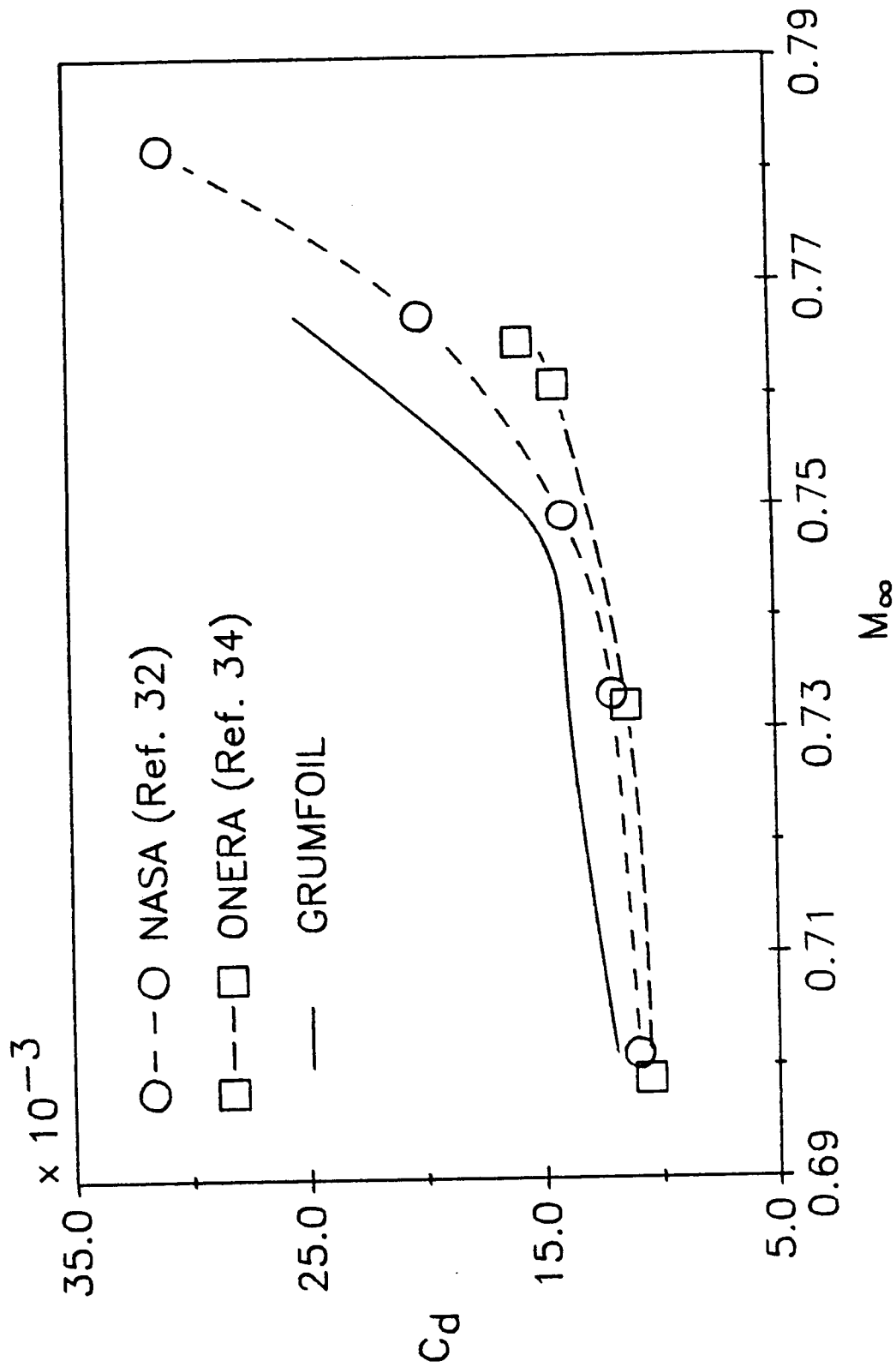
Figure 25. - Drag curves of the French CAST 10 airfoil model as a function of the Mach number from the NASA 0.3-m TCT, ONERA T-2 tunnel, and GRUMFOIL code, $R_c \approx 4 \times 10^6$, $C_l \approx 0.5$, Fixed Transition.
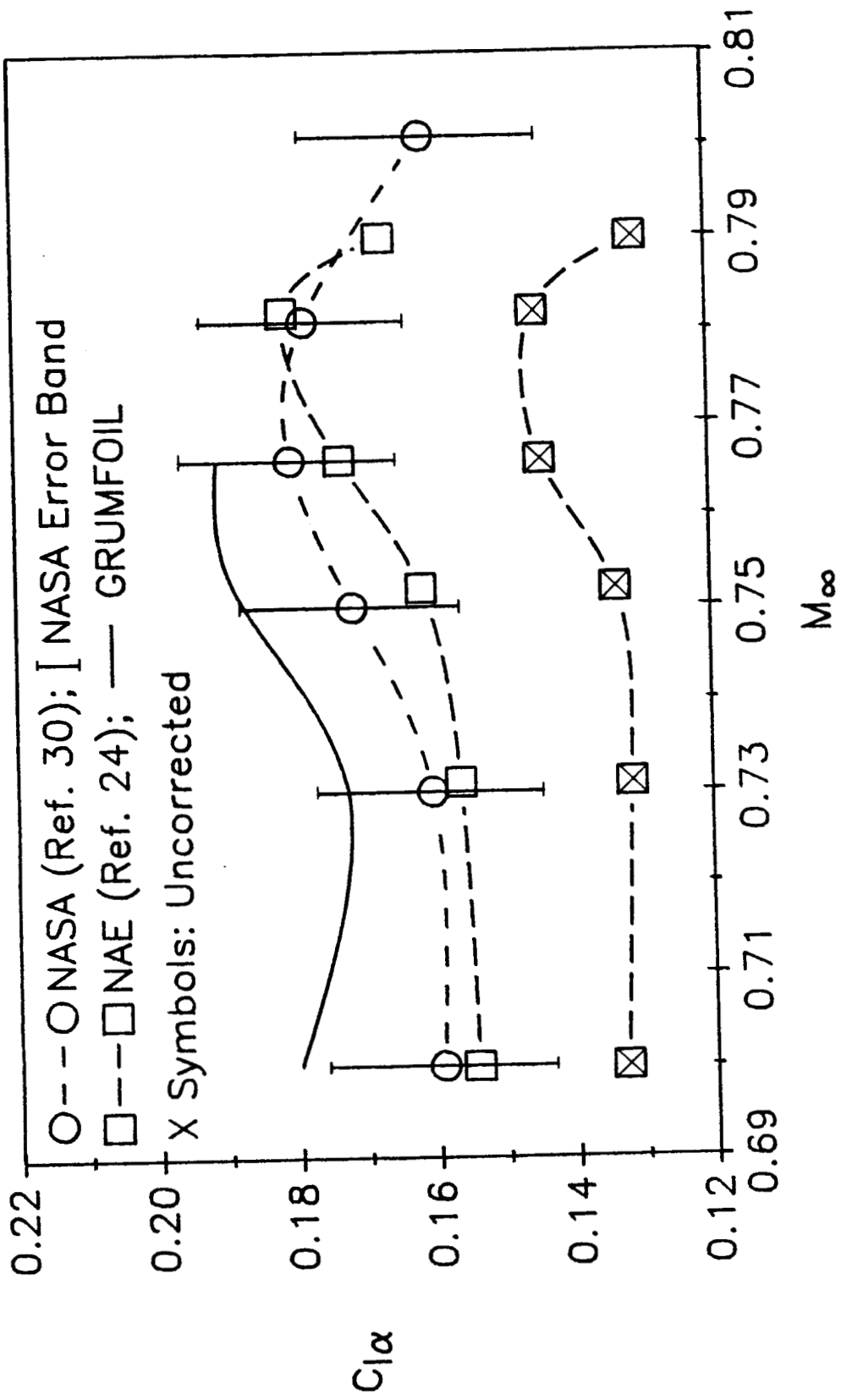
Figure 26. - Lift curve slope of the Canadian CAST 10 airfoil model as a function of the MACH number from the NASA 0.3-m TCT, NAE 5'x5' tunnel, and GRUMFOIL code, $R_c \approx 20 \times 10^6$, Fixed Transition.
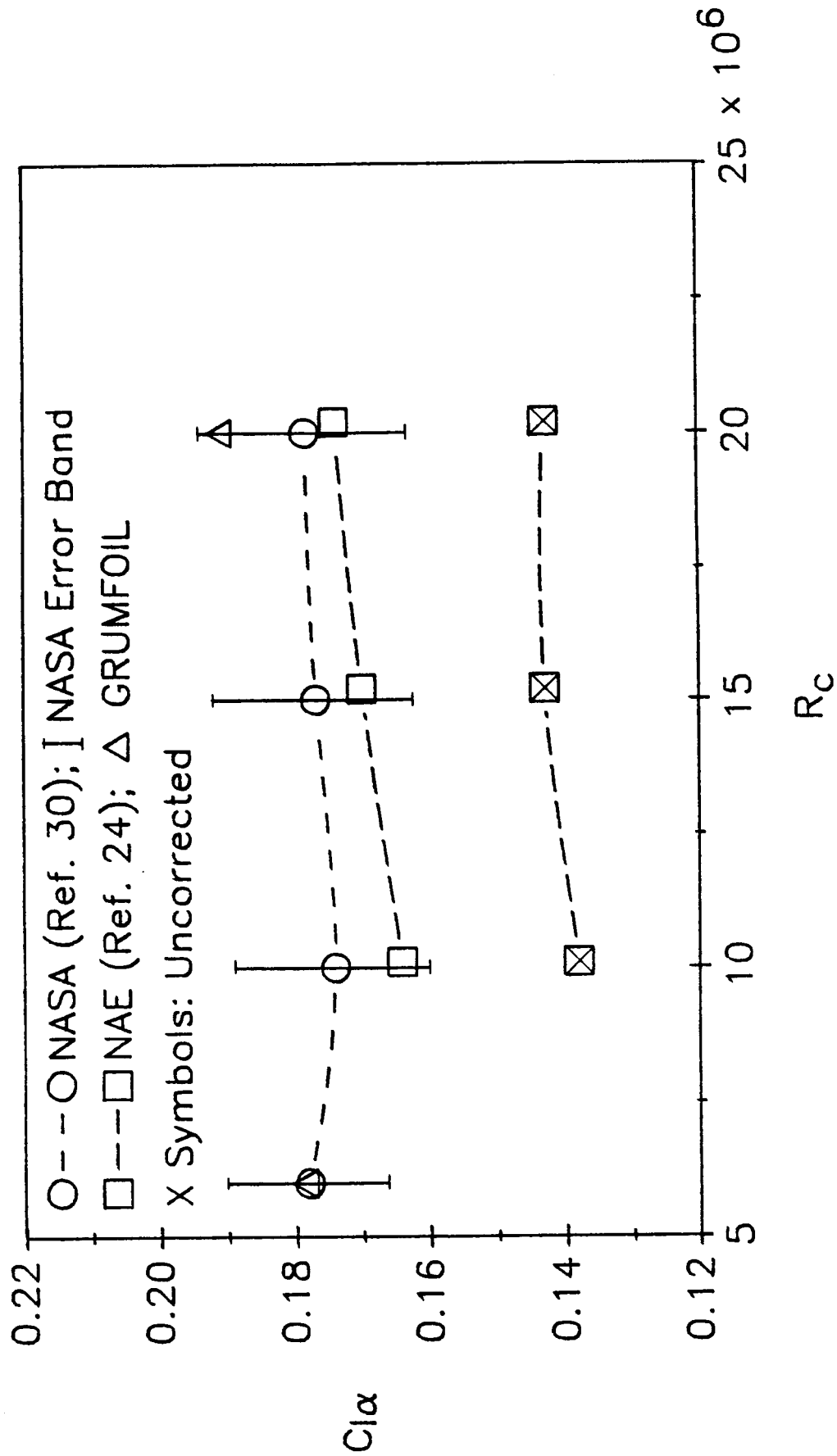
Figure 27. – Lift curve slope of the Canadian CAST 10 airfoil model as a function of the Reynolds number from the NASA 0.3-m TCT, NAE 5'x5' tunnel, and GRUMFOIL code, $M_\infty \approx 0.765$, Fixed Transition.
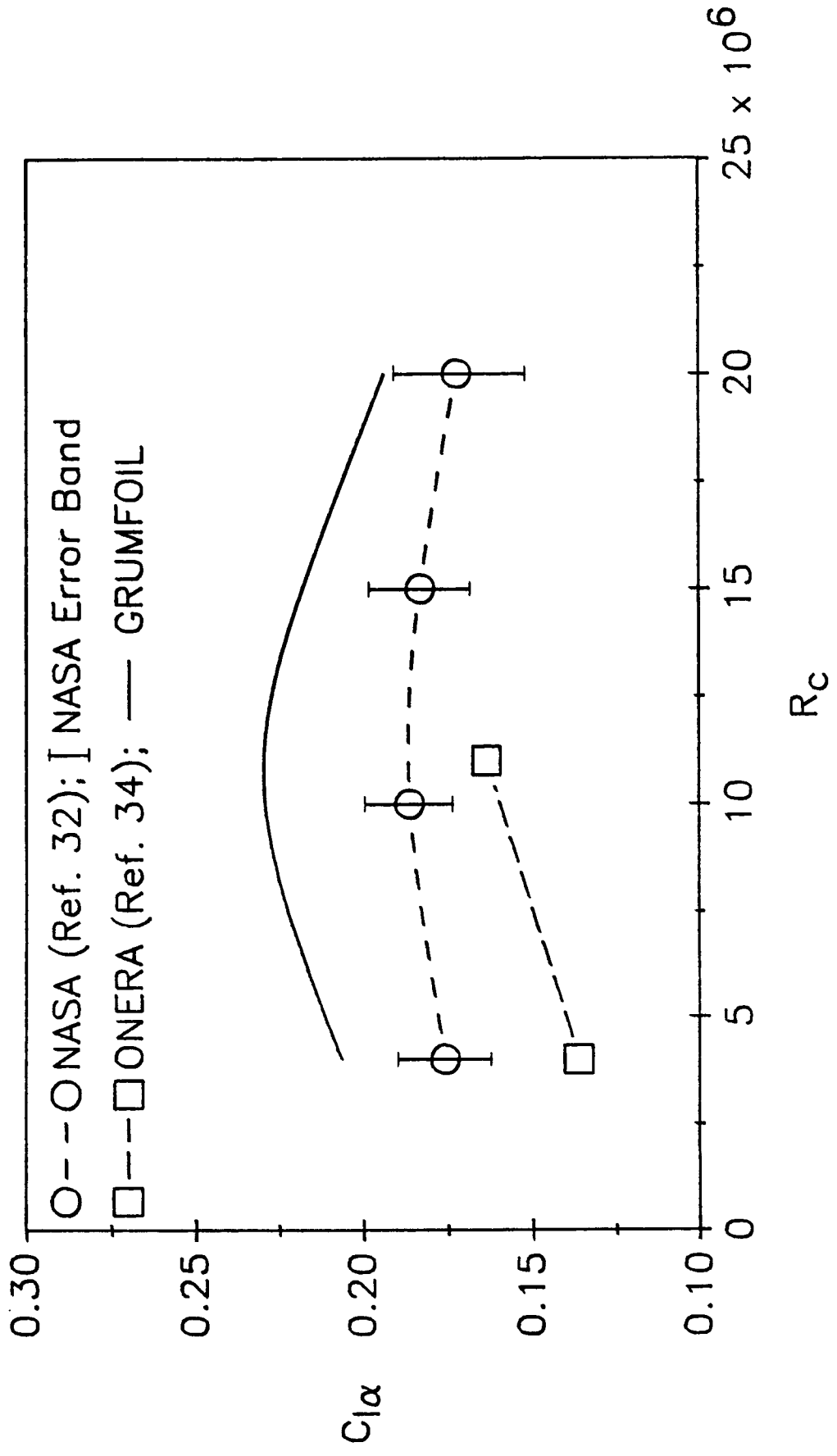
Figure 28. - Lift curve slope of the French CAST 10 airfoil model as a function of the Reynolds number from the NASA 0.3-m TCT, ONERA T-2 tunnel, and GRUMFOIL code, $M_\infty^2 0.765$, Fixed Transition.
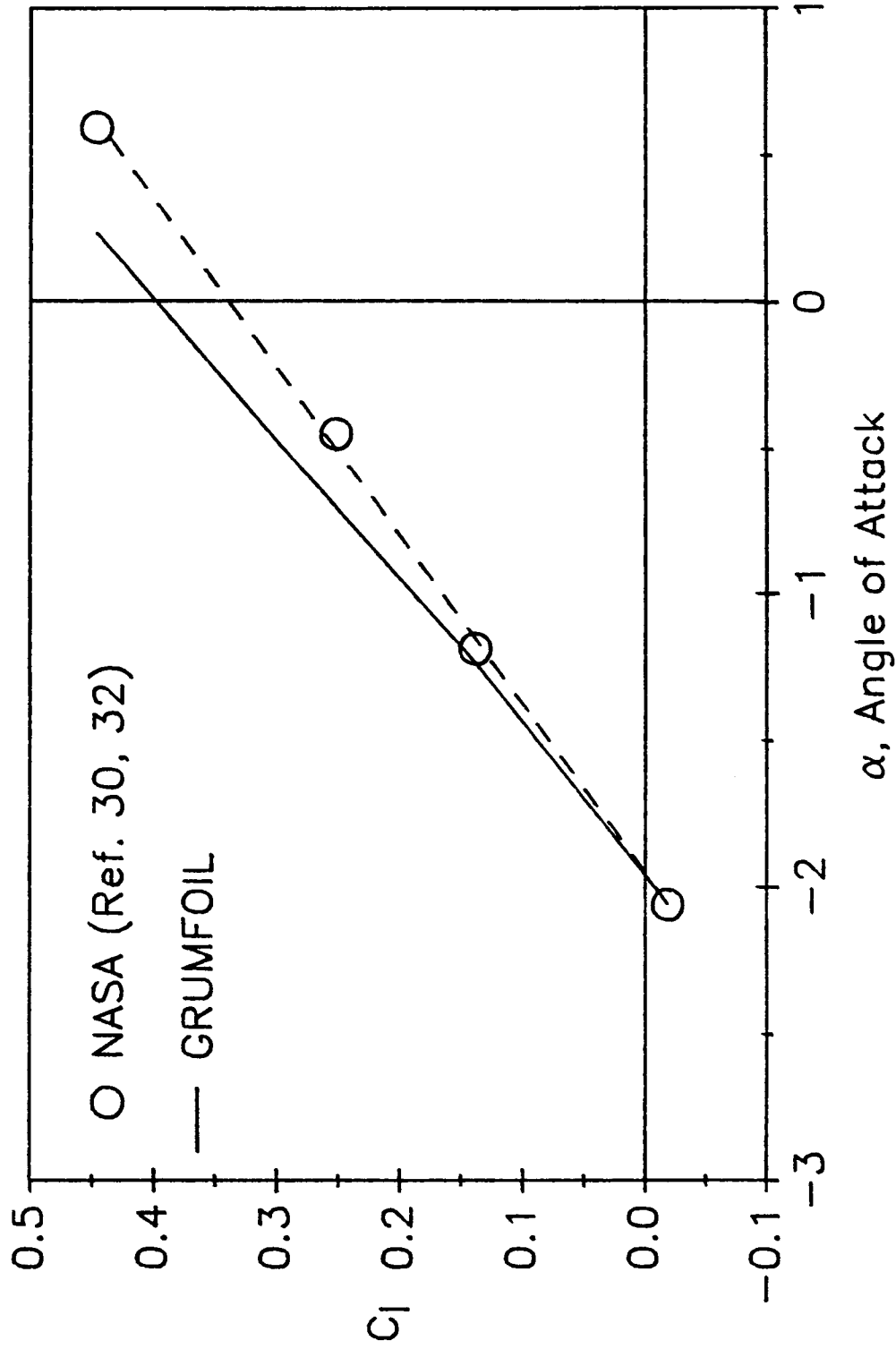
Figure 29. - Experimental lift curve from the NASA 0.3-m TCT and theoretical lift curve from the GRUMFOIL code for the CAST 10 airfoil, $M_\infty \approx 0.765$, $R_c \approx 20 \times 10^6$, Fixed Transition.
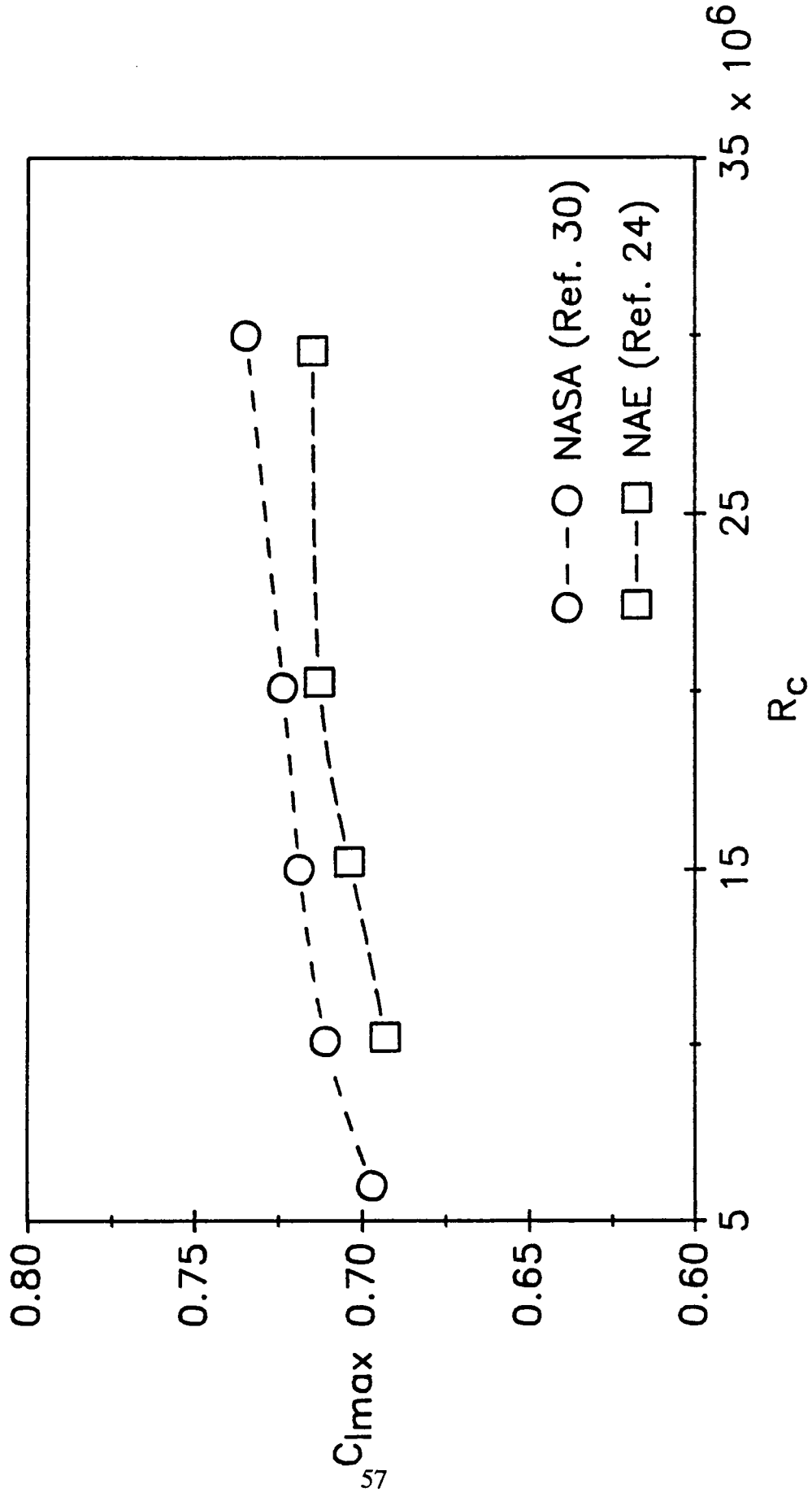
Figure 30. – Maximum lift coefficient of the Canadian CAST 10 airfoil model as a function of the Reynolds number from the NASA 0.3-m TCT and NAE 5'x5' tunnel, $M_\infty ? 0.765$, Fixed Transition.
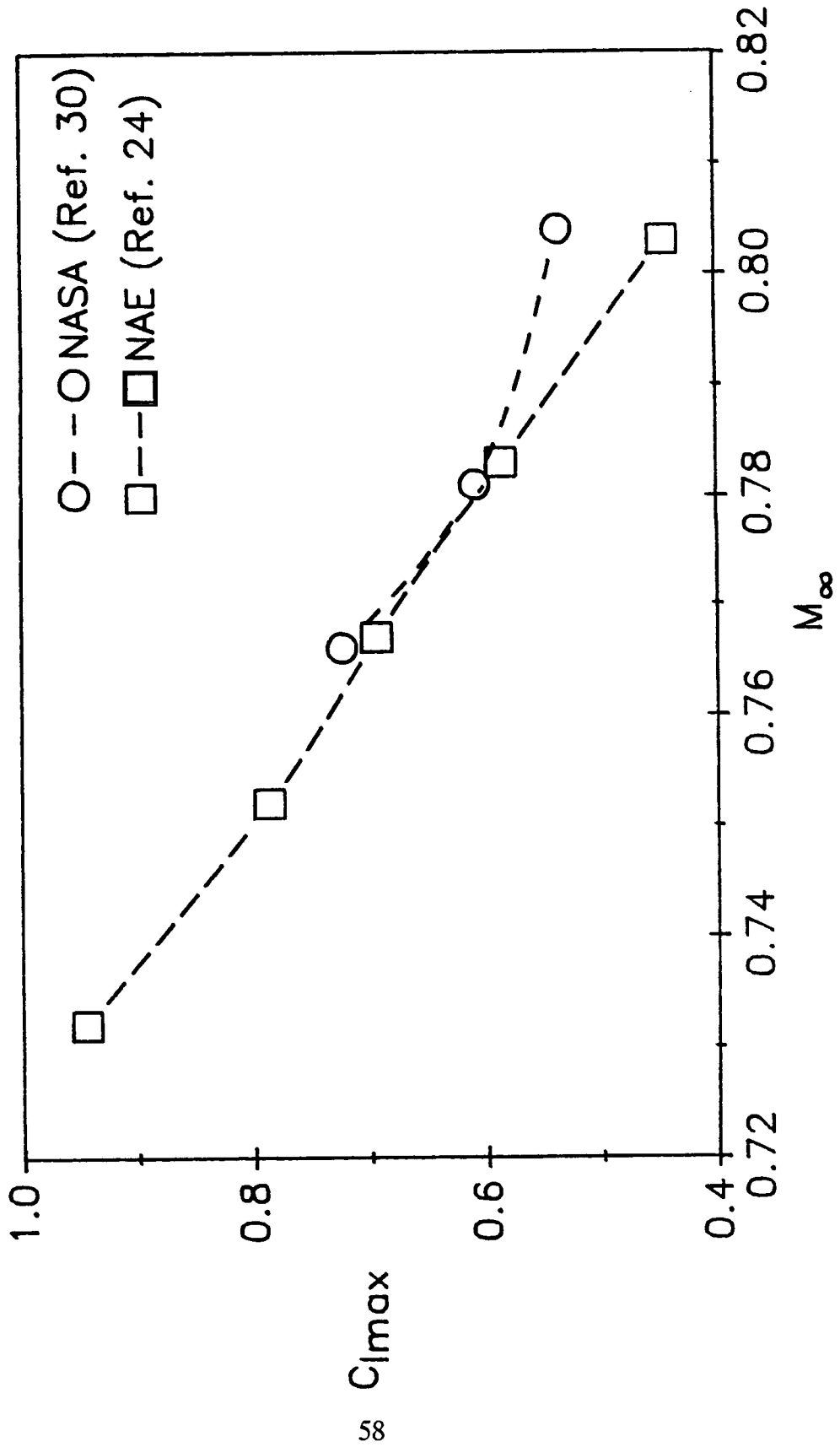
Figure 31. - Maximum lift coefficient of the Canadian CAST 10 airfoil model as a function of the Mach number from the NASA 0.3-m TCT and NAE 5'x5' tunnel, $R_c \approx 20$ x 10^6, Fixed Transition.

Figure 32. - Drag profile of the Canadian CAST 10 airfoil model as a function of the test section span from the NASA 0.3-m TCT and NAE 5'x5' tunnel, $M_\infty \approx 0.765$, $R_c \approx 20 \times 10^6$, $C_l \approx 0.27$, Fixed Transition.
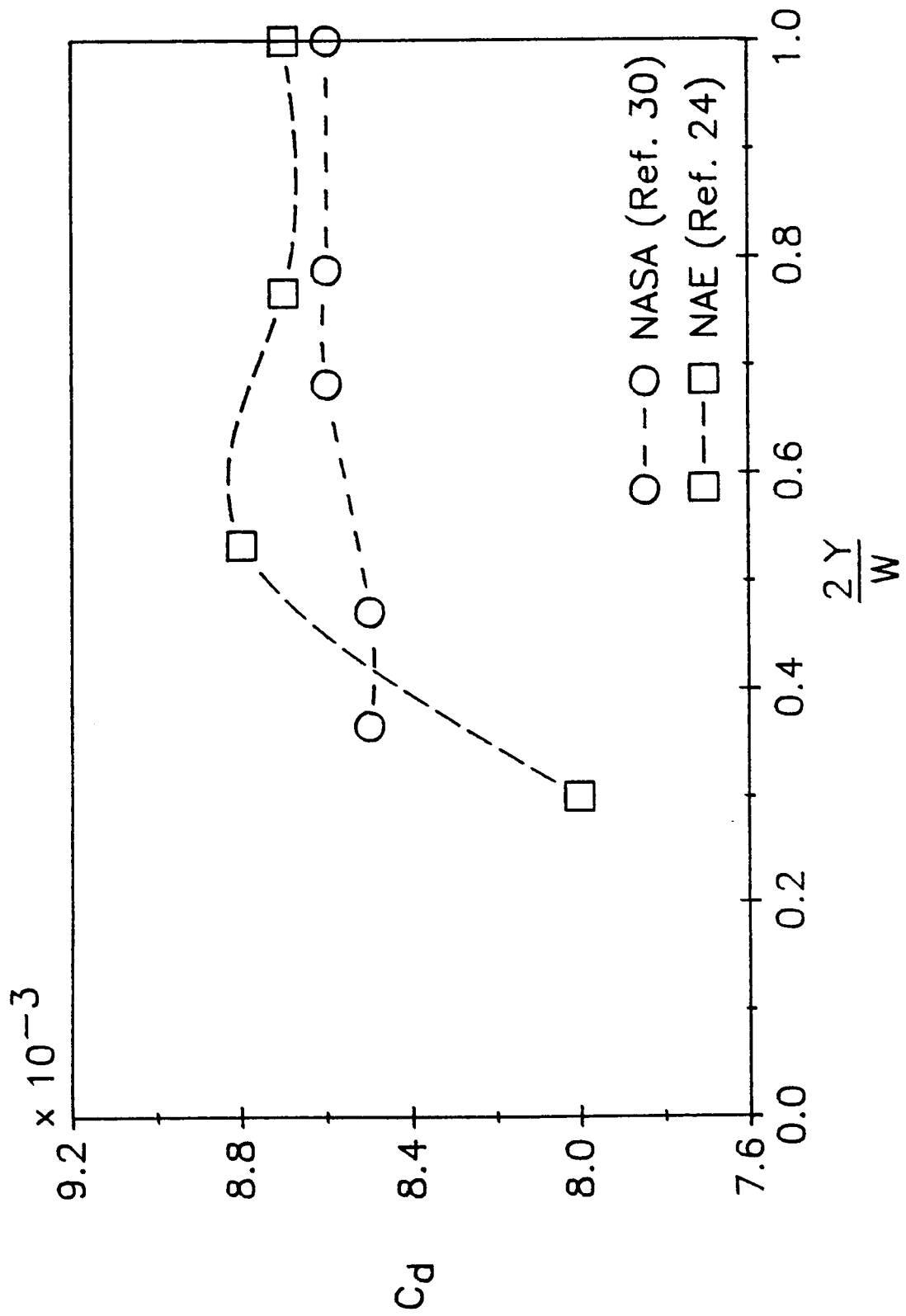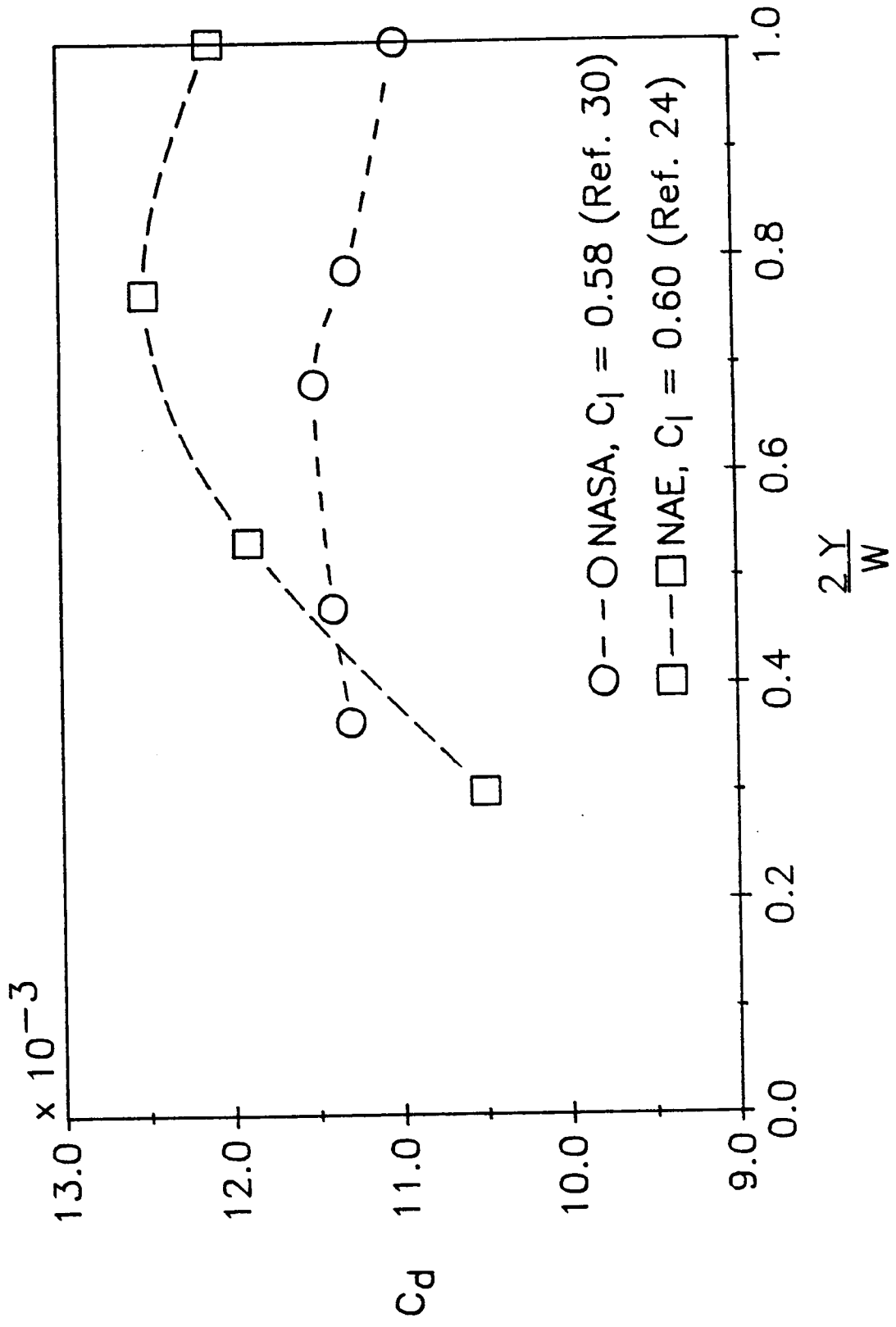
Figure 33. - Drag profile of the Canadian CAST 10 airfoil model as a function of the test section span from the NASA 0.3-m TCT and NAE 5'x5' tunnel, $M_\infty \approx 0.765$, $R_c \approx 20 \times 10^6$, Fixed Transition.

TABLE I

PHYSICAL AND OPERATING CHARACTERISTICS OF THE NASA 0.3-m TCT AND ONERA T-2 TEST SECTIONS

(All lengths are in cm)

	NASA 0.3-m TCT	ONERA T-2
Test section walls	2 Flex. (ceiling and floor) 2 Rigid (side)	2 Flex. (ceiling and floor) 2 Rigid (side)
Test section dimensions (LxHxW)	185x33x33	132x37x39
Flex. wall material	304 Stainless steel	INVAR steel
Jacks per wall	21	16
Jack mechanism	Screw	Hydraulic
Max. jack displacement	7.62 (up), 2.54 (down)	2.5 (up and down)
Min. jack displacement	0.01	0.02
Jack displacement transducer	Linear variable differential transformer	Potentiometric comparator
Accuracy of the jack displacement transducer [cm]	±0.013	±0.005
Jack displacement speed [cm/sec]	0.024	0.6
Pressure taps per wall	18	58
Pressure transducer	Capacitive (Barocell)	Differential (Kulite)
Average accuracy of the pressure transducer [mbar]	±1.5	±2
Test gas	Nitrogen	Air + Nitrogen
Stagnation temperature [K]	80 to 327	100 to 300
Max. stagnation pressure [bars]	6	5
Turbulence level (T=120 K, $M_\infty \approx 0.8$)	0.011	0.0015
Mach number	0.1 to 0.95	0.3 to 1.1
Mach number accuracy	±0.001	±0.002
Reynolds number per meter (T=120 K)	10^7 to 3×10^8	3×10^7 to 3×10^8
Test time [sec]	Continuous	90 to 120
Time of one adaptation step [sec]	≈41	≈7

61

TABLE II

PHYSICAL AND OPERATING CHARACTERISTICS OF THE 2-D, TRANSONIC
TEST SECTION OF THE NAE 5'x5' WIND TUNNEL

(All lengths are in cm)

Test section walls: 2 ventilated (ceiling and floor)
                    2 solid (side)
Test section dimensions (LxHxW): 358x152x38
Ceiling and floor porosity: 8.4%

Test gas: Filtered and dried air
Turbulence level: 0.007 (M_∞ = 0.8)
Max. stagnation pressure: 5 bars
Pressure transducer: Quartz crystal oscillator
Pressure transducer resolution: 0.13 mbar

Mach number: 0.7 to 1.4
Mach number accuracy: ±0.002
Reynolds number per meter: 1.6×10^7 to 6.8×10^7 (M_∞ = 0.75)
Test time: 47 to 4 sec (M_∞ = 0.75)

TABLE III

GEOMETRICAL PARAMETERS OF THE MODEL-WIND TUNNEL SYSTEMS

		NASA	ONERA	NAE
French Model c = 18 cm	W/c	1.8	2.2	/ /
	H/c	1.8	2.1	/ /
Canadian Model c = 23 cm	W/c	1.4	/ /	1.7
	H/c	1.4	/ /	6.7

Report Documentation Page

1. Report No.	2. Government Accession No.	3. Recipient's Catalog No.
NASA CR-181871		

4. Title and Subtitle	5. Report Date
An Evaluation of Three Experimental Processes for Two-Dimensional Transonic Tests	August 1989
	6. Performing Organization Code

7. Author(s)	8. Performing Organization Report No.
Gennaro Zuppardi	
	10. Work Unit No.

9. Performing Organization Name and Address	11. Contract or Grant No.
Gennaro Zuppardi U. of Naples Via Ettore Corcione, 44 Aversa Aversa (CE) Italy	NCC1-47 JIAFS Core Program
	13. Type of Report and Period Covered

12. Sponsoring Agency Name and Address	
National Aeronautics and Space Administration	Contractor Report
Langley Research Center Hampton, VA 23665-5225	14. Sponsoring Agency Code

15. Supplementary Notes

Langley Technical Monitor: Edward J. Ray

16. Abstract

The aerodynamic measurements in conventional wind tunnels usually suffer from the interference effects of the sting supporting the model and the test section walls. These effects are particularly severe in the transonic regime. Sting interference effects can be overcome through the Magnetic Suspension technique. Wall effects can be alleviated by; testing airfoils in conventional, ventilated tunnels at relatively small model to tunnel size ratios, treatment of the tunnel wall boundary layers,or by utilization of the Adaptive Wall Test Section (AWTS) concept. This paper assesses the operating capabilities and results from two of the foremost two-dimensional, transonic, AWTS facilities in existence. These facilities are the NASA 0.3-Meter Transonic Cryogenic Tunnel and the ONERA T-2 facility located in Toulouse, France. In addition, this paper will evaluate the results derived from the well known conventional facility, the NAE 5'X5' Canadian wind tunnel. CAST10/DOA2 Airfoil results will be used in all of the evaluations.

17. Key Words (Suggested by Author(s))	18. Distribution Statement
Adaptive Wall Test Section Boundary Layer	Unclassified - Unlimited Subject Category 09

19. Security Classif. (of this report)	20. Security Classif. (of this page)	21. No. of pages	22. Price
Unclassified	Unclassified	70	A04